SANDIA REPORT
SAND2020-0759
Unclassified Unlimited Release
Printed January 2020

Sandia
National
Laboratories

Six Degrees of Freedom (6DOF) Simulations of Supersonic Fragment Trajectories

Peter D. Yeh

Prepared by
Sandia National Laboratories
Albuquerque, New Mexico 87185
Livermore, California 94550

Issued by Sandia National Laboratories, operated for the United States Department of Energy by National Technology & Engineering Solutions of Sandia, LLC.

Available to DOE and DOE contractors from

U.S. Department of Energy
Office of Scientific and Technical Information
P.O. Box 62
Oak Ridge, TN 37831

Telephone: (865) 576-8401
Facsimile: (865) 576-5728
E-Mail: reports@osti.gov
Online ordering: http://www.osti.gov/scitech

Available to the public from

U.S. Department of Commerce
National Technical Information Service
5301 Shawnee Road
Alexandria, VA 22312

Telephone: (800) 553-6847
Facsimile: (703) 605-6900
E-Mail: orders@ntis.gov
Online order: https://classic.ntis.gov/help/order-methods

ABSTRACT

In this report a process using existing technologies at Sandia National Laboratories (SNL) to simulate the six degrees-of-freedom (6DOF) trajectories of explosive fragments is described and tested. First, aerodynamic forces and moments as functions of orientation are computed using the SIERRA/Aero supersonic flow solver. The forces and moments are normalized and tabulated in a database. Second, this the aerodynamic coefficient database is imported into a 6DOF rigid body dynamics solver in order to compute the resulting trajectories. The supersonic flow simulations are tested for simple geometries and show good agreement with literature values. The simulation procedure is then demonstrated for an example fragment. The results of the example fragment indicate that the distance traveled in the early flight (from 2.5 km/s until decreasing down to 1 km/s) varies widely depending on the initial orientations. The fragment trajectory distribution and steady tumbling rate is explored. The study indicates that a 6DOF analysis will yield information about a spread of possible trajectories, while using an average drag coefficient can only represent the most likely trajectory.

Acknowledgment

This study was spearheaded by Steve Attaway, our late Senior Scientist. His mentorship and guidance was invaluable to the success of this work. In addition, I would like to thank Travis Fisher, Srini Arunajatesan, Bill Haering, Terry Jordan-Culler, John Korbin, Phil Reu, David Peterson, Jason Wilke, Mark Anderson, and everyone else who has helped me and offered their input.

Contents

List of Figures

List of Tables

1. Introduction

Upon detonation of a cased explosive, the case breakup and failure causes fragments of multiple shapes and sizes to be launched outward at high speeds, typically in the supersonic or transonic range. The flight distance, trajectory, and possible tumbling modes of a single fragment depend on the forces and moments experienced by the interaction with the air flow field during the fragment's uncontrolled flight. As transient high-speed airflows may involve highly non-linear, multi-physical phenomena such as shock waves, turbulence, rarefied gas flows, and multi-modal heat transfer, a complete understanding of the trajectory of a single fragment in flight has not been fully established. To this end, the main goal of this study is to use existing computational tools at Sandia National Laboratories (SNL) to compute the trajectory and understand the physics of a single fragment in uncontrolled flight.

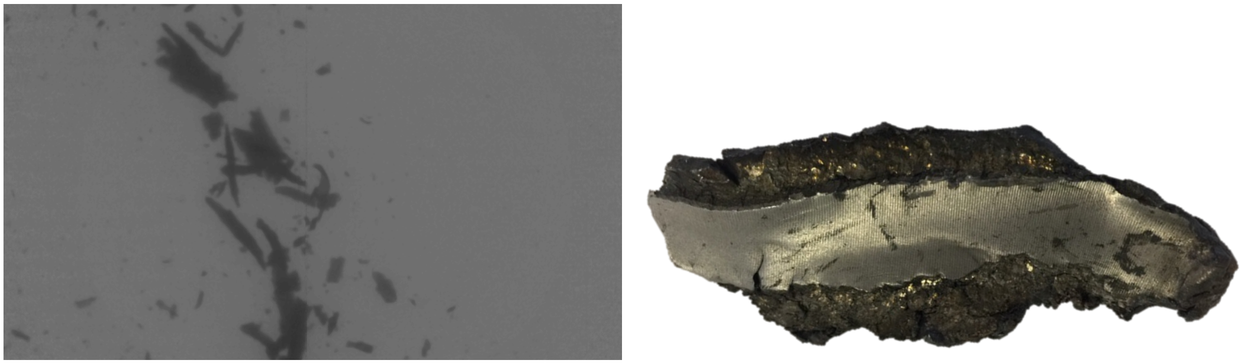

Figure 1-1 (Left) Image of a fragment field resulting from an explosive munition. (Right) Image of a recovered fragment whose complex geometry is representative of typical fragments.

Figure 1-1 illustrates a typical fragment field resulting from an explosive munition as well as the complex geometry of a single recovered fragment. The highest fidelity simulations require these fragments to be used in fully-coupled numerical solvers. However, such simulations are highly expensive. Because of the computational cost and complex fragment geometry, historical estimations of fragment trajectories usually employ a single drag coefficient to characterize the aerodynamic forces. As Figure 1-1 shows, fragment shape and geometry are highly variable, often with large aspect ratios. For such shapes, such as flat plates, the drag may differ by orders of magnitude depending on the plate orientation. Thus, a single drag coefficient approximation may be inaccurate for large aspect ratio fragments. Furthermore, a single drag coefficient does not capture the aerodynamic moments, which induce rotations and tumbling in flight. A more accurate solution methodology is to use steady-state simulations to measure the forces and moments on the fragment during flight as a function of orientation. This quasi-steady approximation is valid if the speed of the fragment rotation is small compared to its flight speed.

In this report a quasi-steady simulation approach for determining fragment trajectories is outlined and shown to be feasible using existing technologies at SNL. First, the problem statement and description of the geometry are described. Then the details of the quasi-steady simulation methodology are explained, and supersonic flow test cases are detailed. Finally, several sample trajectories of example fragment shapes are computed and shown. The simulation results may be validated in future work by an experimental procedure to measure the fragment trajectories for simple shapes. The results of this work opens the possibility of automating the simulation procedure in order to compile a large database of trajectory predictions for a large number of fragments.

2. Problem Statement

2.1. Geometry

An arbitrary-shaped fragment flies through the air as shown in Figure 2-1. Several coordinate systems are defined that characterize the fragment's position. First, a set of inertial axes $(xyz)_I$ is placed at point O, the starting location of the fragment. This coordinate system serves as an inertial reference point for the other coordinate systems. Second, a set of body-fixed axes $(xyz)_b$, is attached to the fragment with its origin at the center of mass, C. The center of mass is located at position $\overrightarrow{r}_C$ relative to the inertial axis. Also, the fragment has instantaneous angular velocity $\overrightarrow{\omega}$, which is consequently the angular velocity of the body-fixed axes. Finally, the fragment is also traveling at instantaneous velocity $\overrightarrow{V}$. A separate wind coordinate system $(xyz)_w$ (not shown in Figure 2-1) characterizes the direction of travel, where $\overrightarrow{V}$ is in the direction of $\hat{x}_w$. The origin of $(xyz)_w$ is also at the fragment's center of mass.

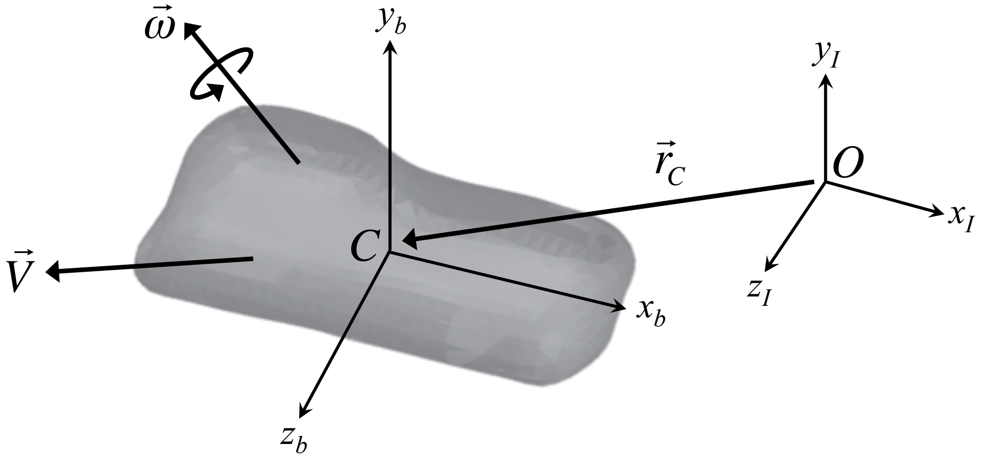

Figure 2-1 Schematic of arbitrary fragment in flight with associated inertial and body-fixed coordinate systems.

The relationship between $(xyz)_I$ and $(xyz)_b$ is characterized by three rotational angles, yaw angle Ψ, pitch angle Θ, and roll angle Φ. To obtain the $(xyz)_b$ axes, rotate the $(xyz)_I$ axes about the z_I-axis by Ψ, then about the new y-axis by Θ, and finally about the new x-axis by Φ. These three angles uniquely identify the fragment orientation relative to the inertial frame. Mathematically, the relationship can be expressed as

$$\begin{bmatrix}\hat{x}_b\\ \hat{y}_b\\ \hat{z}_b\end{bmatrix} = \begin{bmatrix}1 & 0 & 0\\ 0 & \cos\Phi & \sin\Phi\\ 0 & -\sin\Phi & \cos\Phi\end{bmatrix} \begin{bmatrix}\cos\Theta & 0 & -\sin\Theta\\ 0 & 1 & 0\\ \sin\Theta & 0 & \cos\Theta\end{bmatrix} \begin{bmatrix}\cos\Psi & \sin\Psi & 0\\ -\sin\Psi & \cos\Psi & 0\\ 0 & 0 & 1\end{bmatrix} \begin{bmatrix}\hat{x}_I\\ \hat{y}_I\\ \hat{z}_I\end{bmatrix} \tag{2.1}$$

This equation can be succinctly written as

$$\hat{\mathbf{x}}_b = \mathbf{R}\hat{\mathbf{x}}_I \tag{2.2}$$

where $\hat{\mathbf{x}}_i = \begin{bmatrix}\hat{x}_i & \hat{y}_i & \hat{z}_i\end{bmatrix}^T$ are the unit vectors in the coordinate systems (i replaced by b or I) and the rotation matrix $\mathbf{R}$ is the matrix product of the three rotation component matrices. Note that $\mathbf{R}$ is orthogonal so $\mathbf{R}^{-1} = \mathbf{R}^T$, which facilitates computation of the inverse relationship.

Furthermore, the $(xyz)_b$ and $(xyz)_w$ axes are related by a pair of aerodynamic angles, angle of attack α and Euler sideslip angle β_E. The wind axes $(xyz)_w$ can be obtained by rotating the body fixed axes $(xyz)_b$ first by angle α about the y_b-axis and then by angle β_E about the new z-axis. The transformation is given by

$$\begin{bmatrix}\hat{x}_b\\ \hat{y}_b\\ \hat{z}_b\end{bmatrix} = \begin{bmatrix}\cos\alpha & 0 & -\sin\alpha\\ 0 & 1 & 0\\ \sin\alpha & 0 & \cos\alpha\end{bmatrix} \begin{bmatrix}\cos\beta_E & -\sin\beta_E & 0\\ \sin\beta_E & \cos\beta_E & 0\\ 0 & 0 & 1\end{bmatrix} \begin{bmatrix}\hat{x}_w\\ \hat{y}_w\\ \hat{z}_w\end{bmatrix} \tag{2.3}$$

Note that only two rotation angles (α and β_E) are necessary to characterize the fragment's direction of travel with respect to its orientation.

2.2. Equations of Motion

Initial fragment speeds need to experimentally measured or estimated using computational tools. From preliminary data, speeds are estimated to be approximately 2.5 km/s, well into the supersonic range. The forces and moments experienced by a fragment are dictated by its interaction with the surrounding air. In particular, the drag on a bluff body is heavily influenced by the pressure difference, which is affected by the shock wave location, while the drag on a streamlined body is dictated by the turbulent eddies and flow separation point. The velocity, temperature, and pressure field of the airflow surrounding the fragment are governed by the compressible Navier-Stokes equations, whose exact solution at such high Reynolds and Mach numbers are not currently obtainable. Therefore, the widely used Reynolds Averaged Navier-Stokes (RANS) equations in addition to a proper turbulence model provide a useful approximation to compute the flow field.

The surrounding air exerts forces and moments on the fragment, causing the fragment to decelerate, turn, and tumble in a chaotic manner. The exact six degrees-of-freedom (6DOF) dynamics of the fragment can be determined by integrating the Newton-Euler equations of motion:

$$\vec{F} = \frac{\mathrm{d}}{\mathrm{d}t}\left(m\vec{V}\right) \tag{2.4}$$

$$\overrightarrow{M}_C = \frac{\mathrm{d}}{\mathrm{d}t}\left(\bar{\bar{I}}_C \cdot \overrightarrow{\varpi}\right) \tag{2.5}$$

Here, $\overrightarrow{F}$ and $\overrightarrow{M}_C$ are the aerodynamic forces and moments about center of mass C experienced by the fragment. $\bar{\bar{I}}_C$ is the inertia tensor at C represented by a symmetric 3×3 matrix with 6 independent components (see section 3.3).

Solving the Newton-Euler equations with appropriate initial conditions yields the position, velocity, angular orientation, and angular position time histories. Compared to solving for the air flow field, solving the rigid body equations is computationally inexpensive. Thus, if the exact aerodynamic loads and initial conditions were known, the trajectories can be readily computed with high accuracy. The computational challenges arise from determining accurate flow fields and fragment loading conditions.

2.3. Model Assumptions

Note that these set of governing equations carry the assumptions that a) the air is still properly described as a continuum and b) the fragment stays rigid. For small objects moving at hypersonic speeds, the wake directly behind the fragment has high temperature and very low pressure. At sufficiently high temperatures and low pressures, the flow may become rarefied and the continuum model may break down. A scaling estimate shows that this is unlikely. From kinetic theory, the mean free path is proportional to temperature and inversely proportional to pressure: $\lambda_m \sim T/p$. From high speed ballistics simulations, the temperature increase may be up to 10 times and pressure decrease up to 100 times [1]. Using this worst case scenario and noting that the mean free path at STP is 68 nm [2], the mean free path of the gas at its largest is estimated to be 0.068 mm. For a fragment with characteristic length l_c of 1 cm for example, the Knudsen number $\mathrm{Kn} = \lambda_m/l_c$ is 0.0068, which is sufficiently small so that the continuum approximation is still valid.

The second assumption is that the fragment stays rigid during the flight duration of interest. The fragment can only deform significantly if it has either yielded or has melted. As bullets do not significantly deform during flight, it is unlikely that a fragment, if it is a self-contained piece of metal, can deform based on the loading during flight. The yield stress of metals is on the order of 10 MPa, while the stresses experienced by the fragment are on the order of 10-100 kPa, so the fragment is unlikely to yield. One possible exception is a fragment that has two sections connected by a thin filament at the initial stages of flight. In this case it may break apart into two separate fragments. This type of fragment is probably very rare, and its frequency of occurrence may be verified by experimental tests. It is more plausible that the fragment generated from the explosion is at high enough temperature that it has partially melted. In this case, fragment temperature would be higher than the surrounding air temperature (even after local compression), so the heat loss due to convection would likely allow the fragment to solidify quickly.

3. Simulation Procedure

3.1. Quasi-steady Model

As was described in the previous section, the fluid flow is governed by the compressible Navier-Stokes equations, while the fragment flight dynamics is governed by the Newton-Euler equations, assuming that the fragment remains rigid. In theory, the solution to this set of coupled partial differential equations will yield the correct trajectory, but solving the equations directly is currently infeasible due to computational limitations of resolving turbulent eddies. Fortunately, the problem can be made tractable by using modeling assumptions with varying levels of complexity.

The most basic modeling approach is to use a single drag coefficient to characterize the aerodynamic loading. This is best used as a first approximation to the problem. Although the fragment dynamics is indeed dominated by the drag force, this model limits the trajectory to a straight line and also does not take into account rotational degrees of freedom. Fragment shapes may have varying aspect ratios, leading to a complex tumbling motion that would not be captured in this model. This single drag coefficient model is most useful for simpler geometries such as a spin-stabilized bullet in ballistics. On the other hand, the most accurate modeling approach is to solve the coupled equations directly with an appropriate turbulence model as the only simplifying assumption. The advantage of this approach is that the transient dynamics and 6DOF rotational motion can be accurately captured. Despite its accuracy, this procedure is the most computationally expensive by a large margin.

The quasi-steady simulation approach is a compromise. Here, the flow field and 6DOF rigid body dynamics simulations are decoupled. The fragment is held at a fixed orientation and immersed into a uniform supersonic flow at a specified velocity. The aerodynamic forces and moments are computed for this specific orientation. These simulations and aerodynamic load calculations are repeated for all possible unique orientations of the fragment, resulting in a large aerodynamic database consisting of forces and moments as a function of orientation and possibly velocity. Once this database is complete, the trajectory is then integrated forward with the fragment's aerodynamic loading continuously updated from the database.

Note that this quasi-steady assumption is valid if the rigid body tumbles at a relatively slow rate compared to its forward velocity, which is indeed the case for a tumbling fragment traveling at very high forward speeds. Suppose that the fragment has a length scale of 1 cm and is traveling at 1,000 m/s. The angular frequency corresponding to a comparable rotational velocity is about 16,000 rad/s. It has been observed that fragments can tumble on the order of 500 rad/s [3]. Even with this angular frequency doubled to 1,000 rad/s, the maximum velocity due to rotation is still an order of magnitude slower than the fragment's forward velocity. This quasi-steady approach has also been used in a trajectory analysis of aircraft store separation, and it was shown that the fully coupled transient dynamics offered little extra accuracy [4]. Thus, the quasi-steady approach is used to obtain the most accurate solution within a reasonable time-frame.

3.2. Supersonic Flow Simulations

The supersonic flow simulations are performed using SIERRA/Aero, part of the SIERRA Mechanics suite developed at SNL [5]. Aero uses a node-centered finite volume method to solve the compressible Reynolds Averaged Navier-Stokes (RANS) and energy equations on an unstructured three-dimensional mesh [6]. The Shear Stress Transport (SST) model is used as the turbulence model [7]. This model has been demonstrated to be more robust than standard k-ε and k-ω formulations. Although the fragment in most orientations would likely behave like a bluff body in which pressure drag dominates (which can be calculated using an inviscid model), the turbulence model is necessary to account for skin friction drag if the fragment is traveling at a streamlined orientation and also to approximate the flow separation point.

3.2.1. Mesh

The solution for the supersonic flow requires an appropriate mesh for the domain. Pointwise® [8] is used in this study for the mesh generation, although any appropriate meshing tool will suffice. A brief discussion of the mesh is included here, while a more detailed discussion regarding the specific steps in the software is included in Appendix A.

As shown in Figure 3-1, the origin of the body-fixed frame is placed at the center of mass of the arbitrary shaped rigid fragment. The fragment surface is defined by an appropriate triangulation (shown as darker colored lines) with average spacing Δ_i. Far away from the fragment, the far-field surface is a spherical with radius r_f, triangulated with average spacing Δ_f (lighter colored lines). A spherical far-field is conveniently chosen because the goal of the simulations is to build an aerodynamic database depending on the fragment orientation. Instead of generating a new mesh for every fragment orientation, the flow direction is simply changed. The spherical far-field boundary allows for a comparable resolution when the flow direction is changed because the distance from the boundary to the fragment is approximately the same for every flow direction. The solution domain is thus the interior volume in between the far-field surface and fragment. A tetrahedral mesh is used to discretize the interior domain. Near the surface of the fragment, a wedge layer is created by extruding the fragment surface outward by N_e steps of increment Δ_e in order to create a small wedge layer.

Note that the meshing process requires an appropriate geometric representation of the fragment surface in order for triangulation to succeed. For simple shapes, the fragment surface can be created directly in the meshing software or imported from a Computer-Aided Design (CAD) model. For more complicated fragment shapes that are output from computer models or scanned from real fragments, the meshing procedure is much more difficult. Possible solutions are discussed in Appendix A.

3.2.2. Simulation Parameters

With the mesh established, the flow field and aerodynamic forces are determined using SIERRA/Aero, a finite-volume supersonic flow solver [6, 5]. The fluid properties chosen for the

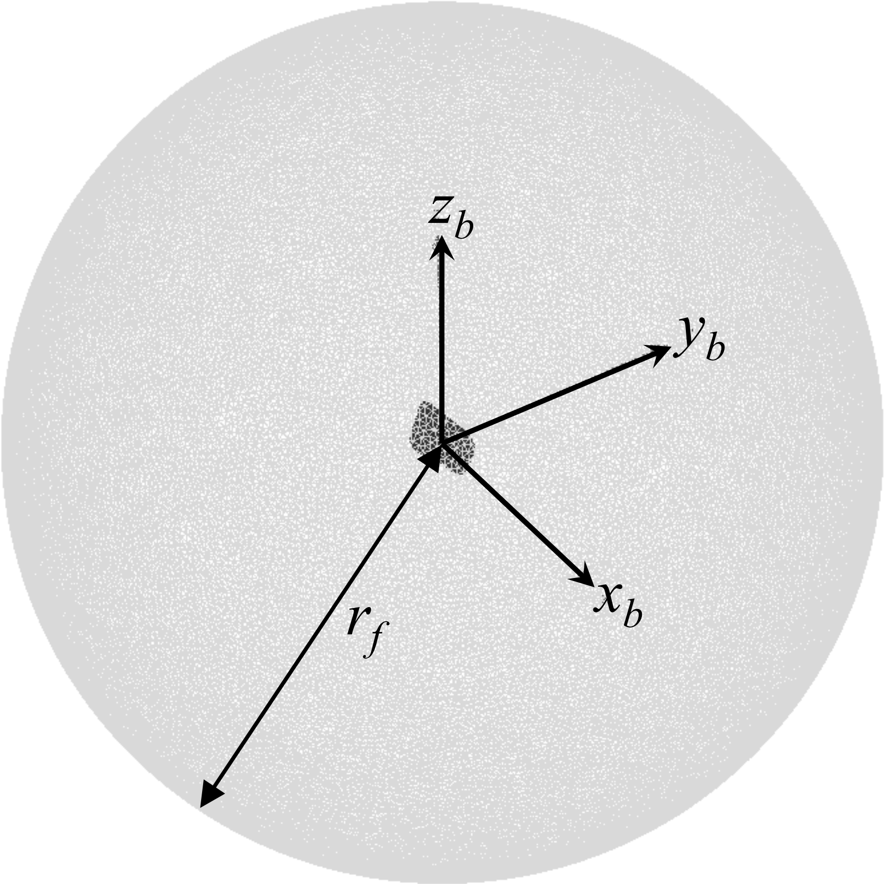

Figure 3-1 Schematic of mesh used in supersonic flow simulations.

simulations are summarized in Table 1. The free stream is initialized with the quantities shown with the $()_\infty$ subscript. Density is calculated using the ideal gas law, $\rho = P/RT$, and the dynamic viscosity is modeled as a function of temperature using Sutherland's law, $\mu = C_1 T^{3/2}/(T + C_2)$. Since the fragment travels in the $\hat{x}_w$ direction, the free stream velocity is therefore initialized in the $-\hat{x}_w$ direction. In terms of orientation angles α and β_E, the flow direction is given by

$$-\hat{x}_w = -\cos\alpha\cos\beta_E\hat{x}_b - \sin\beta_E\hat{y}_b - \sin\alpha\cos\beta_E\hat{z}_b \tag{3.1}$$

The free stream Mach number, Ma_∞, is also specified, leading to free stream velocity $U_\infty = \mathrm{Ma}_\infty\sqrt{\gamma R T_\infty}$. Lastly, the specific turbulent kinetic energy, k, is related to the turbulence intensity, T_u, as $k = 3/2(T_u U)^2$, and the dissipation rate is given by $\omega = \rho k/\mu_t$.

In the simulations a steady state solution (in an averaged sense) is assumed. A local time-stepping method is used to achieve faster convergence. Furthermore, to achieve shorter runtimes with higher accuracy, simulations are performed for a number of time steps (usually 1,000) with first order spatial accuracy, and then continued with second order accuracy. For first order accuracy, the solution value is assumed to be constant across the local control volume. For second order accuracy, a MUSCL scheme determines a linear variation of the solution value across the control

Table 3-1 Fluid properties for simulations

Parameter	Value
Free stream temperature, T_∞	298 K
Free stream pressure, P_∞	101325 Pa
Gas constant, R	287.097 J/kg-K
Heat capacity ratio, γ	1.4
Prandtl number, Pr	0.72
Sutherland constant, C_1	1.458×10^{-6} kg/m-s-K$^{1/2}$
Sutherland constant, C_2	110.4 K
Turbulence intensity, $T_{u\infty}$	0.01
Turbulent viscosity ratio, $(\mu_t/\mu)_\infty$	0.1

volume. In the second order scheme, a van Albada flux limiter is used. To compute the surface advective flux in this compressible finite volume method, a modified Steger-Warming flux function was employed. The no-slip, no-penetration wall boundary condition is applied on the fragment surface, while the far-field boundary condition is applied to the outside spherical boundary surface. These solution options and parameters are all encapsulated in an input file for Aero. A sample input file can be found in Appendix B.

Forces, $\vec{F}$, and moments, $\vec{M}_C$, are found by integrating stresses along the surface of the fragment and are expressed in the body-fixed components. Aerodynamic coefficients are calculated by normalizing the forces and moments:

$$\vec{C}_F = \frac{\vec{F}}{0.5\rho_\infty U_\infty A_r}, \vec{C}_M = \frac{\vec{M}_C}{0.5\rho_\infty U_\infty A_r L_r} \tag{3.2}$$

Here, A_r is a reference area of the fragment, while L_r is a reference length. The components of the aerodynamic coefficients are typically denoted by the following:

$$\vec{C}_F = C_x\hat{x}_b + C_y\hat{y}_b + C_z\hat{z}_b \tag{3.3}$$

$$\vec{C}_M = C_l\hat{x}_b + C_m\hat{y}_b + C_n\hat{z}_b \tag{3.4}$$

These aerodynamic coefficients are generally a function of α, β_E, and also Ma_∞. If Mach number is sufficiently high ($\mathrm{Ma}_\infty \geq 3$), then the aerodynamic coefficients no longer exhibit Mach number dependence [9]. Thus, an aerodynamic database is built up by calculating force and moment coefficients for different sampled values of orientation angles α and β_E.

3.2.3. *Simplification Due to Symmetry*

Generally, an arbitrary fragment has no planes of symmetry. However, simple geometries with symmetry planes may be used for model verification, and exploiting this symmetry can save considerable computational time. To handle this case, consider a plane of symmetry defined by normal vector $\hat{n}_s$. Define a mirrored velocity direction, $\hat{x}_w^m$, which is the fragment velocity direction, $\hat{x}_w$, mirrored across the symmetry plane. Since there is a combination (α, β_E) that maps to $\hat{x}_w$, then there is a corresponding combination (α^m, β_E^m) that maps to the mirrored direction $\hat{x}_w^m$. The mapping between (α^m, β_E^m) and (α, β_E) can be determined based on location of the symmetry plane. The force and moment vectors of the mirrored direction are given by the following:

$$\vec{F}(\alpha^m, \beta_E^m) \cdot \hat{n}_s = -\vec{F}(\alpha, \beta_E) \cdot \hat{n}_s \tag{3.5}$$

$$\vec{F}(\alpha^m, \beta_E^m) \cdot \hat{t}_s = \vec{F}(\alpha, \beta_E) \cdot \hat{t}_s \tag{3.6}$$

$$\vec{M}_C(\alpha^m, \beta_E^m) \cdot \hat{n}_s = \vec{M}_C(\alpha, \beta_E) \cdot \hat{n}_s \tag{3.7}$$

$$\vec{M}_C(\alpha^m, \beta_E^m) \cdot \hat{t}_s = -\vec{M}_C(\alpha, \beta_E) \cdot \hat{t}_s \tag{3.8}$$

Here, $\hat{t}_s$ is any unit vector that is parallel to the symmetry plane and is thus perpendicular to $\hat{n}_s$.

3.3. 6DOF Rigid Body Simulations

The 6DOF rigid body dynamics equations along with the aerodynamic database, described in the previous section, are used to integrate fragment trajectories forward. The Newton-Euler equations (2.4 and 2.5) are solved numerically in this part of the simulation procedure. To facilitate the computations, the equations are rewritten as a set of first order differential equations:

$$\left[\frac{\mathrm{d}\vec{r}_C}{\mathrm{d}t}\right]_I = \vec{V} \tag{3.9}$$

$$m\left[\frac{\mathrm{d}\vec{V}}{\mathrm{d}t}\right]_I = \vec{F} \tag{3.10}$$

$$\bar{\bar{I}}_C \cdot \left[\frac{\mathrm{d}\vec{\omega}}{\mathrm{d}t}\right]_b = \vec{M}_C - \vec{\omega} \times \left(\bar{\bar{I}}_C \cdot \vec{\omega}\right) \tag{3.11}$$

The inertia tensor can be represented by a 3×3 symmetric matrix and is defined by

$$\bar{\bar{I}}_C = \begin{bmatrix} I_{xx} & I_{xy} & I_{xz} \\ I_{xy} & I_{yy} & I_{yz} \\ I_{xz} & I_{yz} & I_{zz} \end{bmatrix} = \iiint_V \rho_s(x_b, y_b, z_b) \begin{bmatrix} y_b^2 + z_b^2 & -x_b y_b & -x_b z_b \\ -x_b y_b & x_b^2 + z_b^2 & -y_b z_b \\ -x_b z_b & -y_b z_b & x_b^2 + y_b^2 \end{bmatrix} \mathrm{d}x_b \mathrm{d}y_b \mathrm{d}z_b \tag{3.12}$$

These components of the inertia matrix are computed with respect to the body fixed basis. Also, the fragment density ρ_s may not be constant but can vary within the fragment volume V.

With the multiple coordinate systems, it is important to clarify the reference frames and basis vectors associated with the quantities in these equations. Equations (3.9) and (3.10) are both solved in the inertial frame. The time derivative, denoted using the $[\ ]_I$ brackets, is with taken respect to the inertial frame ($\hat{\mathbf{x}}_I$ basis vectors are constant as usual). Fragment center of mass position and velocity vectors are written in terms of the inertial basis vectors:

$$\vec{r}_C = x_C \hat{x}_I + y_C \hat{y}_I + z_C \hat{z}_I \tag{3.13}$$

$$\vec{V} = V_x\hat{x}_I + V_y\hat{y}_I + V_z\hat{z}_I \tag{3.14}$$

In (3.10), the aerodynamic force vector $\vec{F}$ is however expressed in body-fixed coordinates (equation 3.3) in the aerodynamic database and will need to be transformed to inertial coordinates using (2.1).

The rotational dynamics equation (3.11) is solved in the body-fixed frame in order that the inertia tensor stays constant in time. The time derivative is taken with respect to the body-fixed frame and written with $[\;]_b$ brackets to indicate that the $\hat{\mathbf{x}}_b$ basis vectors are held constant. All of the quantities in the equation are already expressed in body-fixed coordinates. In particular, the angular velocity vector is written as

$$\vec{\omega} = p\hat{x}_b + q\hat{y}_b + r\hat{z}_b \tag{3.15}$$

However, note that $\vec{\omega}$ is the angular velocity of the fragment *with respect to the inertial frame* despite being expressed in body-fixed basis vectors.

An additional set of equations, Poisson's kinematic equations, relate yaw Ψ, pitch Θ, and roll Φ to angular velocity components.

$$\frac{\mathrm{d}\mathbf{R}}{\mathrm{d}t} = \mathbf{R}\mathbf{W} \tag{3.16}$$

$$\mathbf{W} = \begin{bmatrix} 0 & -r & q \\ r & 0 & -p \\ -q & p & 0 \end{bmatrix} \tag{3.17}$$

Here, $\mathbf{R} = \mathbf{R}(\Psi, \Theta, \Phi)$ is the rotation transformation matrix as defined in (2.2). The nine components are solved separately although they are not all independent.

Equations (3.9)–(3.11) and (3.16) are discretized in time and solved numerically using a fourth order Runge-Kutta scheme with a constant time step Δ_t as part of an internal 6DOF rigid body dynamics code. In order to solve the equations, 12 initial conditions are required — 3 vector components each for initial position, velocity, angular orientation, and angular velocity. It is recommended that the initial position be set to $(0,0,0)$, the location of the inertial frame. The other quantities are either estimated, sampled, or predicted by shock physics simulations. In addition, the following mass and geometric properties of the fragment must be known: center of mass location, total mass, and inertia tensor components about the center of mass.

3.4. Summary of Steps

The quasi-steady simulation procedure to determine the fragment trajectories can be summarized in the following steps:

1. Represent the fragment as a CAD geometry or stereolithography (STL) file. If a real fragment is scanned into a high resolution STL file, the resulting wire mesh may be too coarse and must be smoothed in order to facilitate the meshing process.

2. Use Pointwise or another meshing tool to generate the appropriate mesh for the supersonic flow simulations. The meshing software must be able to export the mesh in the EXODUS file format.

3. Import the mesh into SIERRA/Aero and apply an initial uniform supersonic flow across the interior domain. Sampling the entire space of possible fragment orientations, solve for the steady state RANS solution and compute the aerodynamic coefficients for each orientation. Create a data file that contains the aerodynamic coefficient database as functions of orientation angles.

4. Import the aerodynamic database into the 6DOF rigid body dynamics solver. This will determine the external forces and moments acting instantaneously upon the fragment in flight. Using known fragment material properties, compute the fragment trajectories by applying known or estimated initial conditions. Multiple initial conditions may also be sampled in order to establish the trajectory as a function of initial orientation.

3.5. Model Limitations

In addition to the limitations inherent in the modeling assumptions from section 2.3, there are further modeling considerations to be aware of. Additional limitations include the following:

- The model solves for the steady state drag at different orientations of the fragment, so transient flow dynamics and rotational damping effects are not captured. This is mitigated again if the rotation of the fragment is slow compared to the free stream fluid velocity.

- The quasi-steady model does not allow for the drag or lift due to spin for a fragment with an axisymmetric geometry. This is a transient effect that will not be captured from the steady state flow simulations. Fortunately, actual fragment geometries are never perfectly axisymmetric.

- If the aerodynamic coefficient database is not a function of Mach number, then the trajectories may only be reliable if the Mach number does not fall below approximately 2 or 3. Near Mach 1, the speed of sound, the drag coefficients increase. In order to capture this regime the functional relationship between the aerodynamic coefficients and Mach number must be determined either by creating a larger database or establishing a correlation.

- The actual fragment geometries are likely to have rough surfaces and jagged edges. The supersonic flow solver is unable to resolve the fine details without an extraordinarily large computational domain. The fragment geometries must be smoothed before meshing. Because the drag is most likely dominated by pressure, the surface details should contribute little to the aerodynamic forces.

4. Supersonic Flow Test Cases

While SIERRA/Aero is a mature internal code that has been extensively tested and validated, it was worthwhile to perform supersonic flow simulations on test cases of simple geometries. In particular, the flow past a bluff body, such as a general shaped fragment, can have complex structures. These tests verified that the computational software has been capable of capturing the flow structures and determining the aerodynamic loads accurately. The test cases in this section include a two-dimensional flow past a cylinder and a three-dimensional flow past a cube. In these cases the drag was computed and compared to reported literature values.

4.1. 2D Supersonic Flow Past Cylinder

The first test case considered is the flow past a circular cylinder in a two-dimensional domain. The flow past this simple geometry is a canonical external flow problem used as a first step of validation. Furthermore, the important features of bluff body external compressible flow are highlighted. A circular cylinder of diameter $D = 6$ mm was held in place in a uniform flow with Mach number 1.7. This particular Mach number was chosen to compare to a drag coefficient reported in literature. Instead of a spherical domain in 3D as described in section 3.2, a circular domain was used instead. The cylinder boundary had spacing $\Delta_i = 0.192$ mm, domain radius $r_f = 4.5D = 27$ mm, and outer boundary spacing $\Delta_f = 0.5$ mm. This mesh had a total of 14635 nodes and 28832 cells. Multiple grids had been tested, but this was the smallest grid to yield accurate results.

The flow was initiated in the $\hat{x}_b$ direction (see section 2.1 for the coordinate definitions). The drag was computed as $C_D = F_x/0.5\rho_\infty U_\infty^2 D$. Simulations were performed using 1 node with 16 processors in Skybridge with 10,000 timesteps with the first 1,000 using a first order accurate scheme and the rest second order. Runtime was 3 minutes. The computed drag coefficient was 1.402, which is in excellent agreement with the reported literature value of 1.3962 [10]. The results show that using a circular shaped mesh is indeed sufficient to capture the drag on a cylinder and that wake refinement is unnecessary.

In order to verify the accuracy of the solution field, the flow field variables were visualized. Contours of Mach number, temperature, pressure, and turbulent kinetic energy are plotted in Figure 4-1. The Mach number contours display the expected pattern for a supersonic flow past a bluff body. Far upstream of the cylinder, the flow is at the free-stream velocity. A steady bow shock is formed in front of the cylinder where the flow velocity rapidly decreases to subsonic speeds. A stagnation point is found at the front tip of the cylinder, and a subsonic turbulent wake with some recirculation extends behind the cylinder. As the fluid turns past the cylinder, the flow undergoes Prandtl-Meyer expansion, rising to velocities faster than the free-stream. This faster flow rapidly decelerates back to the free-stream velocity past the trailing edge shock, which extends at an angle from the wake.

At the front of the cylinder, the air is compressed, resulting in higher temperature and pressure. Behind the cylinder, the pressure is lower in the wake, leading to considerable pressure drag, which is expected for a bluff body. The air temperature is increased to approximately 500K

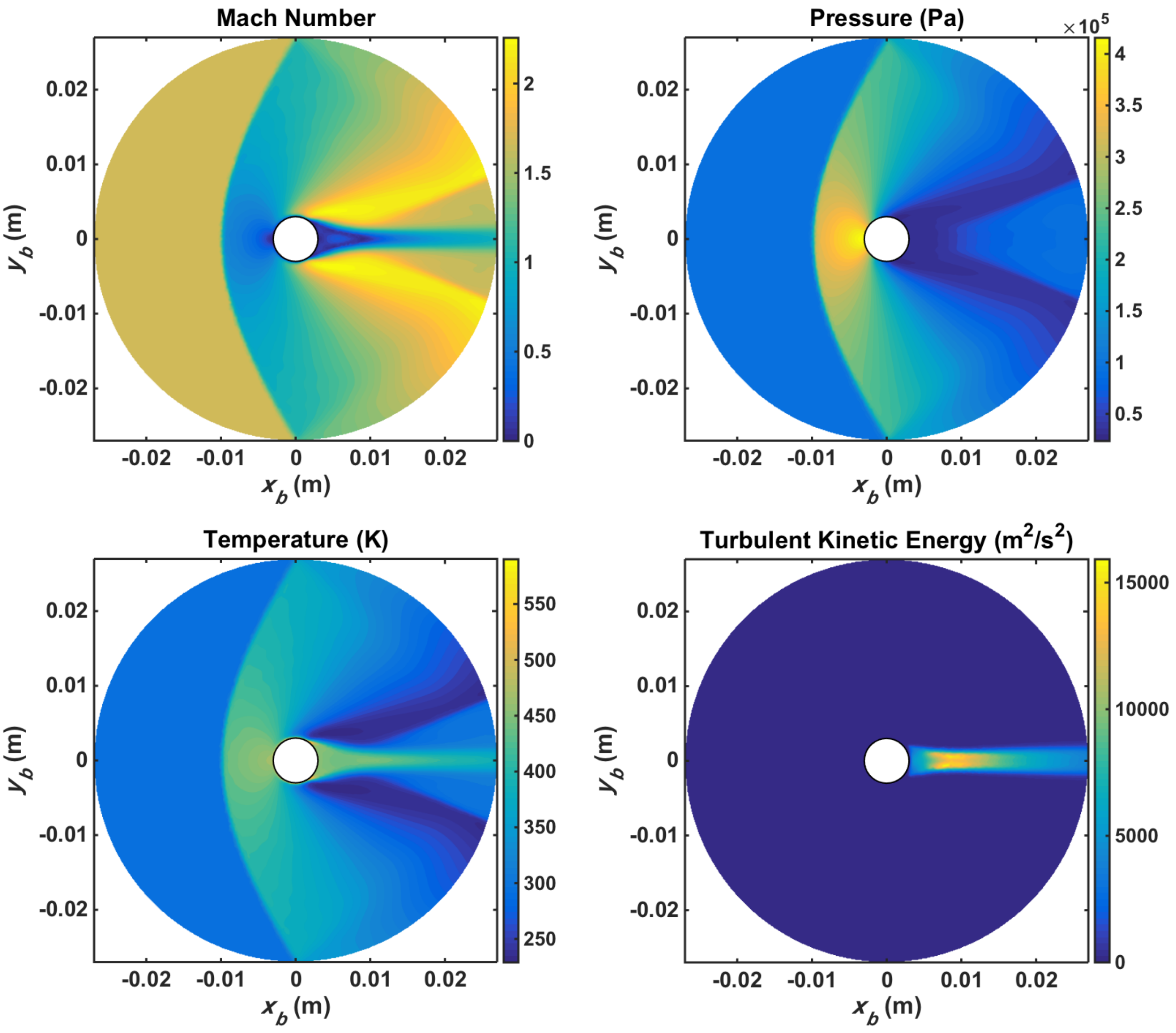

Figure 4-1 Contours of flow variables for a supersonic flow past a 2D cylinder at Mach 1.7.

around the cylinder. At these relatively slower supersonic speeds, the heating is therefore not significant, but the temperature is expected to increase substantially with higher Mach number flows. Finally, contours of the turbulent kinetic energy are shown, which roughly indicate the location of strong turbulent eddies. As expected, the turbulence is only significant in the wake behind the cylinder. There should be a separating turbulent boundary layer near the surface of the cylinder, which this current resolution may not resolve. Fortunately, this does not appear to significantly affect the computed drag coefficient because the drag is dominated by pressure. Thus, the flow structures are found to match well with physical expectations, and the flow simulation accurately determines the aerodynamic loading.

4.2. Supersonic Flow Past Cube

The next test case considered is a Mach 3 flow past a cube in three dimensions. This test demonstrated the capabilities of the flow solver to handle shapes with sharp edges. Furthermore, the results provided insight on how orientation could affect drag and flight trajectory on a three dimensional object. As described in section 3.2, the cube was placed at the center of a spherical domain, and the space between the cube and edges of the sphere form an unstructured tetrahedral mesh. A wedge layer was extruded from the cube surface for refinement and improved accuracy. The cube side length and mesh properties are outlined in Table 4-1. The cube size is comparable to that of a fragment.

Table 4-1 Cube and mesh properties.

Parameter	Value
Side length, s	3 cm
Interior mesh spacing, Δ_i	0.05 cm
Radius of spherical domain, r_f	13.5 cm
Far-field mesh spacing, Δ_f	0.2 cm
Wedge layer spacing, Δ_e	0.01 cm
Number of extrusion steps, N_e	20

The flow direction is varied in order to probe how the aerodynamic forces change as the orientation changes. Because of the cube symmetry (see section 3.2), the angles in ranges $\alpha = [0°, 90°]$ and $\beta_E = [0°, 90°]$ are sufficient to characterize all possible orientations. Equally spaced points of 11.25°, spanning the entire domain of angle pairs, are sampled. As described above, the force and moment coefficients are expressed in the body fixed basis $(xyz)_b$ when output from the flow solver. However, the results can be analyzed more clearly when the coefficients are transformed in the wind coordinate basis $(xyz)_V$. In this coordinate system, $C_{x,V}$ is the drag coefficient, and $C_{y,V}$ and $C_{z,V}$ are side force coefficients. The force and moment coefficients in the wind basis are shown as contour plots as functions of α and β_E in Figure 4-2.

First, consider the case when $\beta_E = 0°$. When $\alpha = 0°$, the flow points directly in the middle of a face. As α increases, the flow direction rotates, catching the face at an angle, until $\alpha = 45°$, when the flow is completely edge-on. In this case, the drag coefficient for edge-on flow is surprisingly the highest for constant β_E. One would expect that the edge-on orientation be relatively more streamlined, leading to a lower drag coefficient. This is true, but the higher drag is due to the increase in projected area. As mentioned earlier, the drag is normalized by the single face area. Correcting the drag coefficient for the projected area leads to a drag coefficient of 1.2, which matches quite well with a literature value of about 1.15 [9]. The more-streamlined geometry cannot overcome the increase in projected area which leads to a larger drag. Note that the drag coefficient $C_{x,V}$ should also be symmetric about $\alpha = 45°$, which provides an immediate accuracy check.

When $\alpha = \pi/4$, the drag coefficient reaches a maximum that corresponds to $\beta_E = \cos^{-1}\left(\sqrt{6}/3\right) \approx 35.3°$. This is the "corner-on" case in which the flow direction is parallel

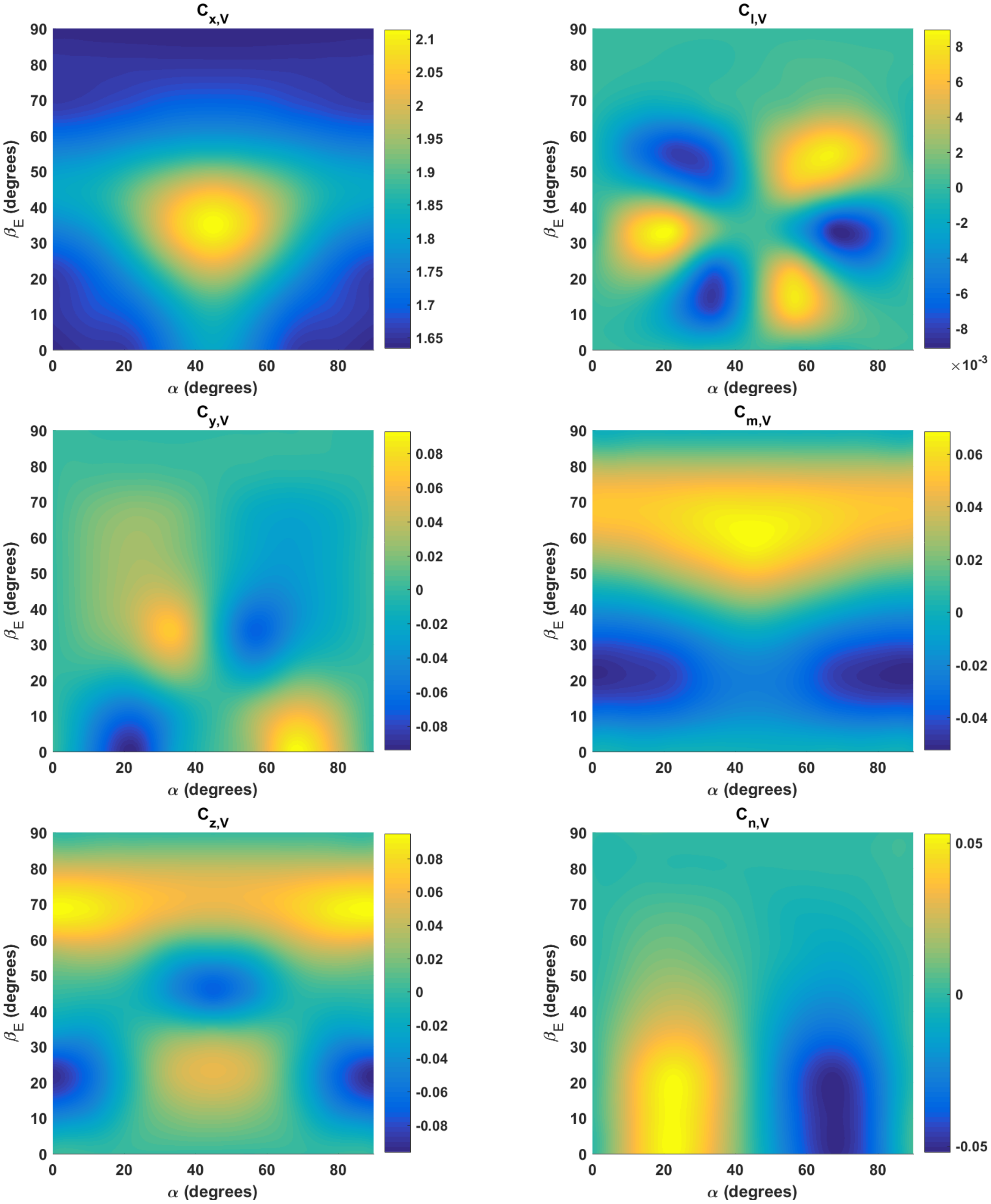

Figure 4-2 Force and moment coefficients in the wind coordinate basis on a cube as a function of orientation angle. In particular, $C_{x,V}$ is the drag coefficient.

to a line connecting the corner to the cube center. In this particular orientation, the projected area is maximized. This shows that the projected area has the most important influence on drag (for a cube, at least) when changing orientation. Therefore, when a cube flies through the air, it will experience the least drag resistance face-on because it has the minimum projected area, which is an interesting and counter-intuitive result.

Side force coefficients $C_{y,V}$ and $C_{z,V}$ as functions of orientation are also shown in Figure 4-2. These forces arise due to the asymmetry of the cube from the viewpoint in the flow direction and act to deviate the cube from a straight-line trajectory. They are much smaller (about 2 orders of magnitude) than the drag, but these forces are not insignificant and may to lead to $O(10\text{ m})$ flight path deviations for every 200 – 300 m traveled. Finally, the moment coefficients $C_{l,V}$, $C_{m,V}$, and $C_{n,V}$ are responsible for the rotation in flight.

5. Analysis of Fragment Trajectories

The supersonic flow test cases considered fragments such as circles and cubes whose shapes have multiple symmetries. Actual fragments, either from explosive tests or shock physics simulations, can have arbitrary shape. The robustness of the simulation procedure (described in section 3) is demonstrated in this section by applying it to a test fragment with a complicated shape whose schematic was shown above in Figure 2-1. This representative fragment was numerically generated from a shock physics simulation. Its length is 4.4 cm, and it is composed of steel with a density of 7,800 kg/m^3. The flight dynamics of this single fragment is studied in this section using our simulation methodology described in earlier sections. Detailed material and mesh properties are shown below in Table 5-1. Note that the body-fixed coordinate system is placed at the fragment's center of mass but is not concurrent with the principal axes of inertia.

Table 5-1 Material and mesh properties for test fragment.

Parameter	Value
Mass, m	45.0 g
x-Moment of Inertia, I_{xx}	25.0 g-cm^2
y-Moment of Inertia, I_{yy}	79.2 g-cm^2
z-Moment of Inertia, I_{zz}	57.8 g-cm^2
xy-Product of Inertia, I_{xy}	3.74 g-cm^2
yz-Product of Inertia, I_{yz}	2.61 g-cm^2
xz-Product of Inertia, I_{xz}	11.5 g-cm^2
Interior mesh spacing, Δ_i	0.073 cm
Radius of spherical domain, r_f	20.0 cm
Far-field mesh spacing, Δ_f	0.3 cm

The six aerodynamic force and moment coefficients associated with this fragment were computed and are shown below in Figure 5-1. As in Figure 4-2, which showed the aerodynamic coefficients for a cube, the contour plots are shown as a function of angle of attack α and Euler side-slip angle β_E. These force and moment coefficients serve as a lookup table for the 6DOF solver.

5.1. Trajectory Uncertainty Due to Initial Orientation

Fragment flight is chaotic and small changes in initial orientation can greatly affect the resulting trajectory. To better understand these uncertainties, 100 fragment trajectories were simulated with

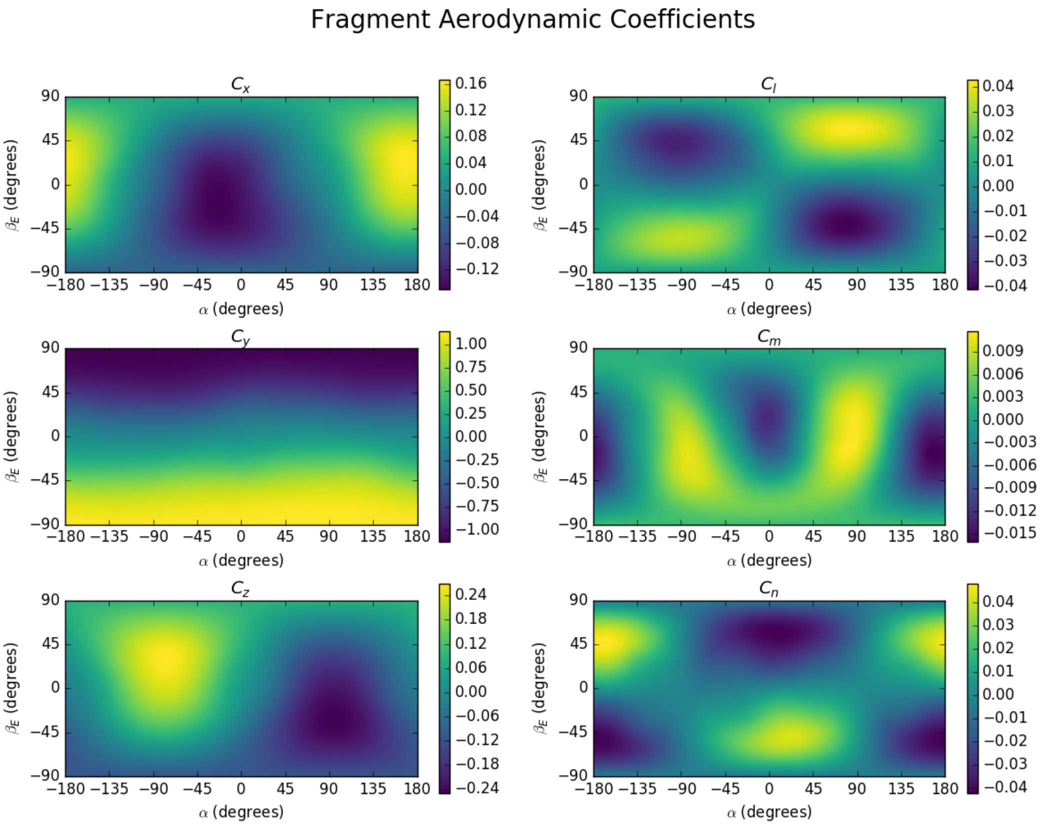

Figure 5-1 Aerodynamic force and moment coefficients for sample fragment.

random initial orientations. All possible initial orientations were assumed to be equally likely, and the fragment has initial horizontal (x–direction) velocity of 2.5 km/s. Here, the fragments have no initial angular velocity (this effect will be discussed later in section 5.3). The trajectory calculations were stopped when the horizontal velocity reached 1 km/s.

5.1.1. 3D Trajectories

The 3D trajectories are plotted in Figure 5-2. On the left, the isometric view shows the variation of possible chaotic trajectories depending on initial orientation. Note that the axes are not to scale, so the fragments travel mostly in a straight line over approximately 100 m with about 2 m of drift. The lateral drift trajectory is shown on the right side of Figure 5-2. This view looks in the $-x$–direction. The plot shows that fragments can follow a curved path in any direction, including upwards. In a practical sense, these fragments would fly much farther than originally expected. The lateral drift is examined below in section 5.1.3.

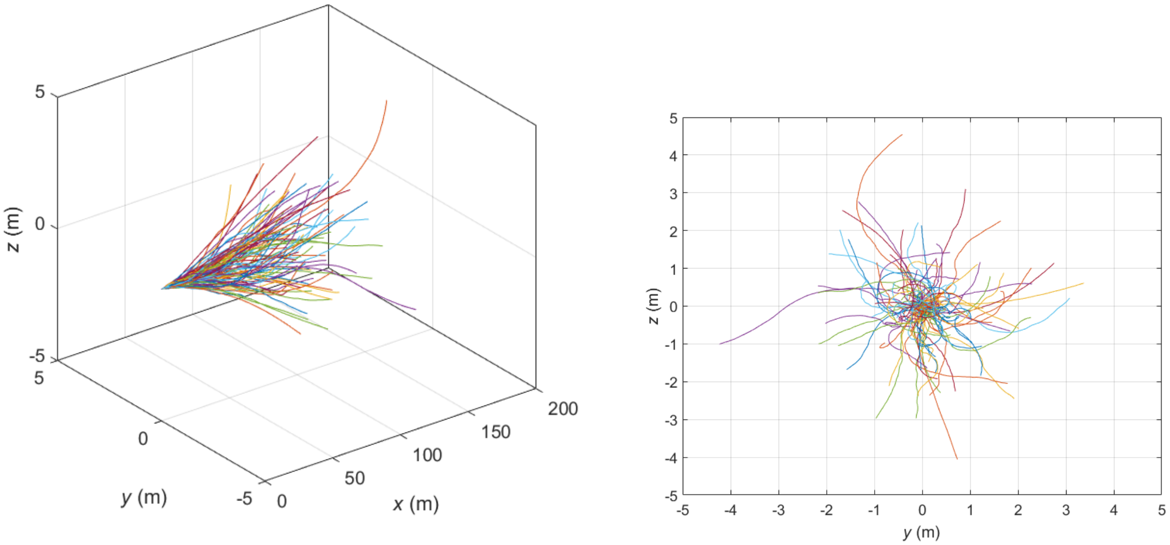

Figure 5-2 Left: Isometric view of fragment trajectories with 100 different initial orientations. Trajectories ended when velocity reached 1 km/s. Right: *yz*–plane view illustrates how far fragments can drift laterally.

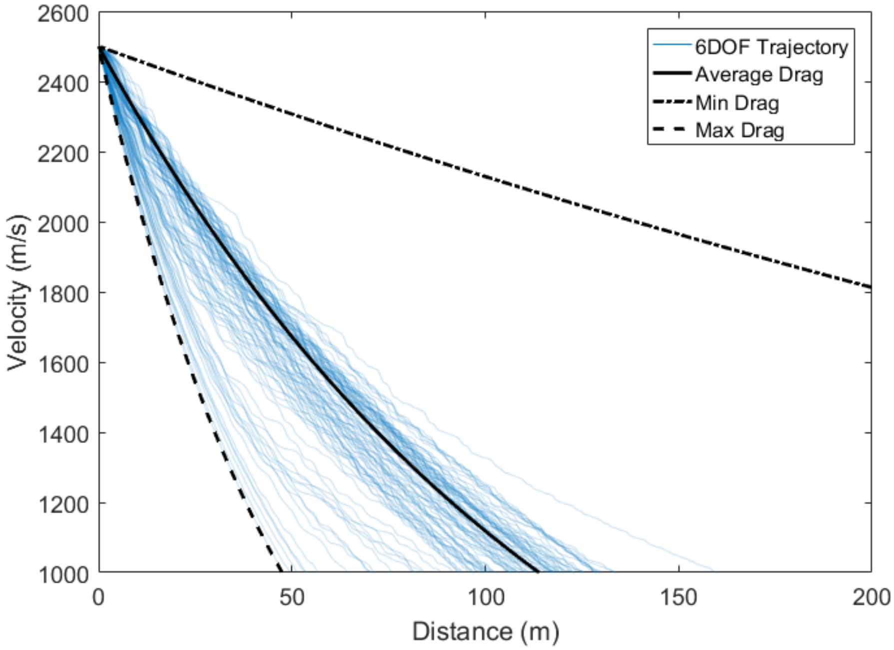

Figure 5-3 Fragment velocity as a function of distance for 100 randomly sampled initial orientations. Trajectories are bounded by minimum and maximum drag of the fragment. Single DOF trajectory (dark line) using the average drag approximates the most likely trajectory, although the spread is wide.

5.1.2. Fragment Velocity vs. Distance Traveled

In Figure 5-3, the fragment horizontal velocity is a plotted as a function of distance for all 100 samples of initial orientation (shown in blue). High variability was found for the trajectories — the distance traveled after decelerating to 1 km/s varied from approximately 45 m to 160 m. A histogram representing the distribution of fragment flight distances is shown in Figure 5-4. The most likely distances ranged from approximately 90 m to 130 m. The histogram also shows that the distribution is skewed to the left, which suggests that fragments have a higher tendency to fly shorter distances than fly longer distances.

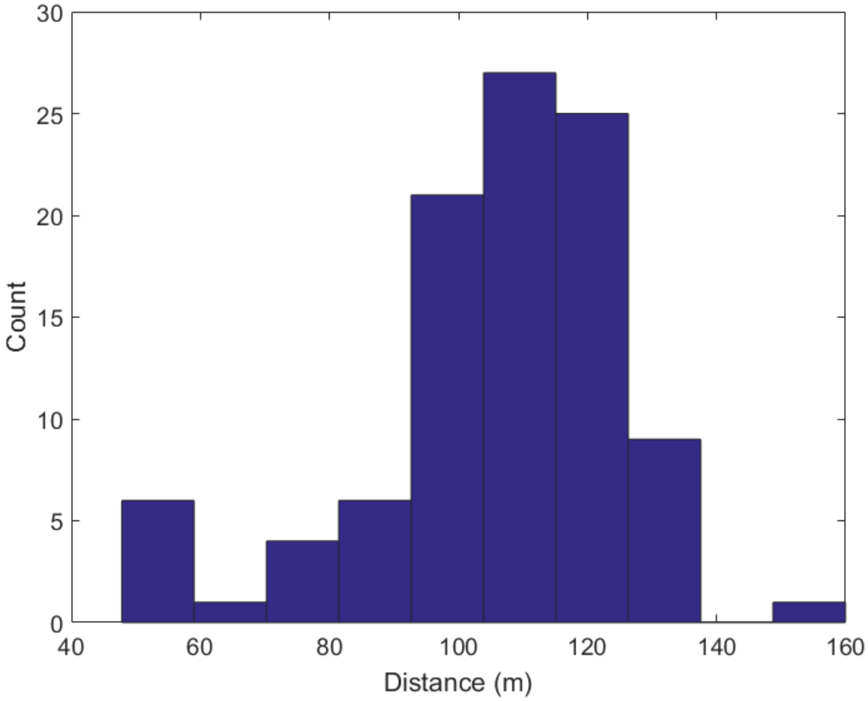

Figure 5-4 Distribution of horizontal distance traveled for single fragment after decreasing speed to 1 km/s.

A comparison with a single DOF approximation (Appendix C) is also presented in Figure 5-3. Based on the aerodynamic coefficient surfaces shown in Figure 5-1, the maximum, minimum, and average drag coefficients were computed. Using these coefficients, the single DOF trajectories were computed and are shown as dark lines. As expected, the maximum and minimum drag coefficients bound the possible trajectory space. While some fragment trajectories approach the lower bound, the upper bound stretches to approximately 600 m (not shown). This opens the possibility that fragments could fly nearly that far, although based on the observed trajectories, the farthest fragments do not come close to this bound. The average drag coefficient single DOF trajectory is also shown in Figure 5-3. This trajectory is found to approximate the most likely trajectory and distance traveled (Figure 5-4). Thus, a single drag coefficient, which is used in current methods for characterizing fragment transport, is useful for predicting the most likely trajectory and serves as a first approximation. The 6DOF simulations are able to extend the information presented by a 1DOF model, capture the spread of probable trajectories, and measure uncertainties associated with fragment velocity and distance.

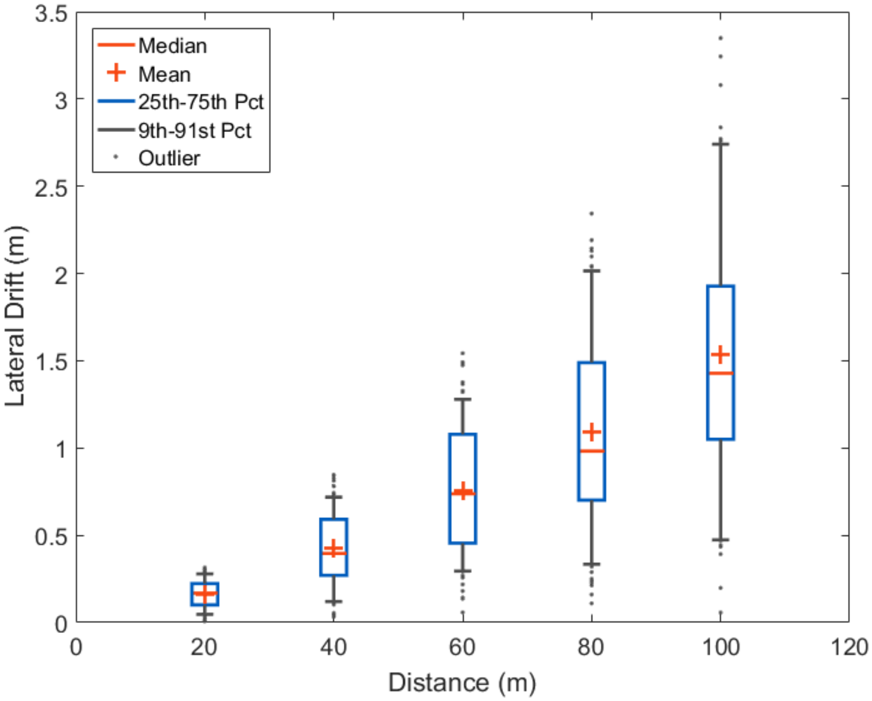

Figure 5-5 Box plots showing distributions of lateral drift at various distances for 100 fragment trajectories with varying initial orientation.

5.1.3. Lateral Drift vs. Distance Traveled

The lateral drift, δ, is defined as the perpendicular distance away from a straight-line trajectory. Specifically,

$$\delta(x) = \sqrt{y(x)^2 + z(x)^2} \tag{5.1}$$

Figure 5-5 shows a box plot of the lateral drift distributions every 20 m in the 100 fragment trajectories. The mean and max drift increase nearly quadratically with distance. The mean drift ratio ranges from 0.8% for 20 m to 1.5% for 100 m, and the max drift ratio ranges from 1.6% for 20 m to 3.3% for 100 m. For longer distances though, the rate of increasing drift may be faster than quadratic. The distributions are observed to be nearly symmetric with some fragments staying near a straight-line trajectory and others curving away. For farther distances, the distribution exhibits a slight right skew, which is expected as some outlier fragments may follow a highly curved path away from a horizontal trajectory.

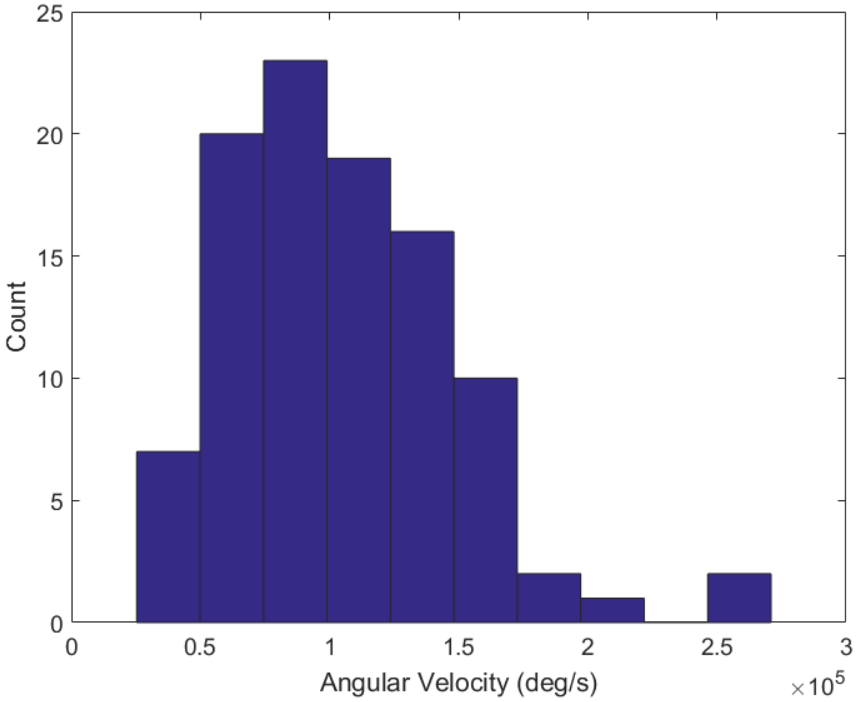

Figure 5-6 Distribution of final angular velocities for 100 trajectories sampled with different initial orientations after slowing down to 1 km/s from 2.5 km/s.

5.2. Analysis of Fragment Tumbling

In addition to capturing the spread of 3D trajectories, the 6DOF simulations are capable of capturing the rotational dynamics of the fragment flight. Rotations affect the trajectory because the aerodynamic forces, particularly drag, depend on the fragment orientation with respect to its direction of travel. The fragment may possibly also reach a spin-stabilized state and travel farther than expected.

As a first step in assessing the rotational dynamics, the final angular velocity (magnitude) was measured for each fragment for the set of simulations described in the previous section. The final angular velocity magnitude is recorded when the center of mass velocity reaches 1 km/s. While not shown explicitly, most of the fragments have reached a steady tumbling frequency by this time in the trajectory. In Figure 5-6, a histogram of the final angular velocities is shown, and the final angular velocity is found to follow a distribution centered around 100,000 deg/s with a spread ranging from approximately 50,000 deg/s to 250,000 deg/s (or approximately 0.14 to 0.69 rev/ms). Regardless of the differing fragment trajectories, the angular velocities are found to be in the same order of magnitude.

The angular velocity can be written out as vector components in a body-fixed basis as $\vec{\omega} = p\hat{x}_b + q\hat{y}_b + r\hat{z}_b$. In order to understand how the fragment tumbles during the trajectory, these components are plotted as "rotation trajectories" in space in Figure 5-7. One rotation trajectory represents the path traced out by the tip of the fragment angular velocity vector (with its base at the origin) as it evolves in time. For example, a single point in this angular velocity space indicates a rotation about a fixed axis. The dark lines indicate the principal axes of inertia, where the numbered subscripts are ordered by decreasing values of the principal moments of inertia (I_1 corresponds to the maximum moment of inertia).

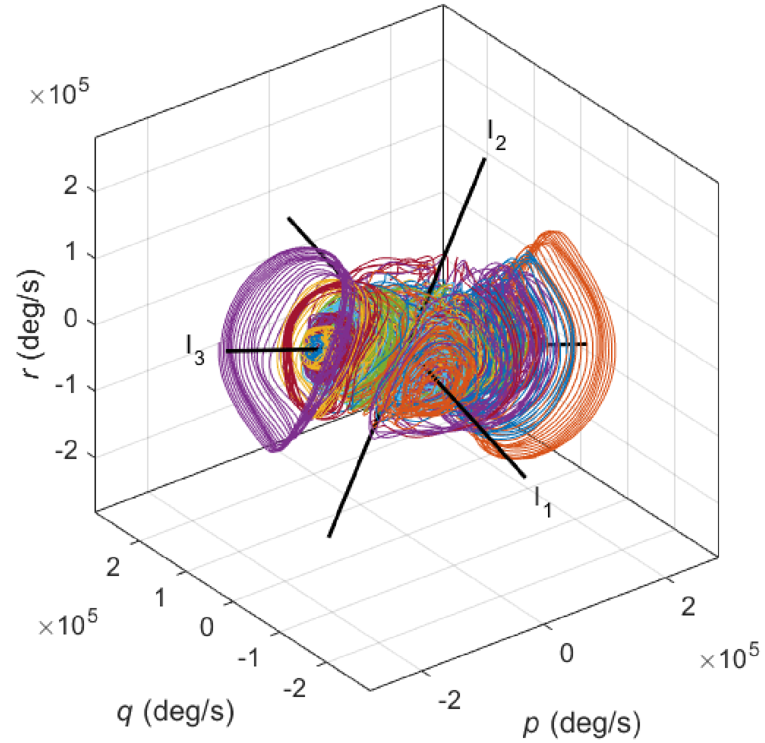

Figure 5-7 Vector components of angular velocity (body-fixed basis) plotted in angular velocity space. Rotation trajectories converge to near-circular orbits around maximum and minimum principal inertia axes (I_3 and I_1, respectively), while they diverge about the middle principal axis I_2.

The rotation trajectories tend to converge to a near-circular orbit around the maximum and minimum principal axes of inertia, (I_1 and I_3, respectively). The angular velocities are found to be higher near I_3, which is expected as this is the axis with the least resistance to rotations. Interestingly, the rotation trajectories diverge about the middle principal axis I_2. By performing a stability analysis of the rigid body equations of motion under torque-free conditions, it can be shown that rotations about the intermediate axis are indeed unstable [11]. This is a well-known phenomenon in satellite design, sometimes called the "Tennis Racquet Theorem." Though the fragment in flight is clearly experiencing torque, this condition still appears to hold and the fragment does not tumble about the intermediate axis. The rotation trajectories clearly show that while fragments tumble chaotically (in the sense of initial condition sensitivity), the steady rotations in late-time flight follow a semblance of structure, especially those that converge to near-circular orbits about the principal axes.

The nature of the circular orbits in the rotation trajectories can be explained with a simple system shown in Figure 5-8a. Here, assume a rigid body is spinning about its body-fixed $\hat{x}_b$–axis with a rotation rate s. The rigid body also undergoes steady precession about a fixed axis $\hat{Z}$. Then the angular velocity can be written as the following:

$$\vec{\omega} = s\hat{x}_b + \Omega\hat{Z} \tag{5.2}$$

Converting to body-fixed basis vectors,

$$\vec{\omega} = s\hat{x}_b + \Omega\sin(st)\hat{y}_b + \Omega\cos(st)\hat{z}_b \tag{5.3}$$

When this angular velocity vector is plotted in space (Figure 5-8b), the tip traces a circle about the spin axis. The angular velocity can be decomposed into spin and precession components as shown. Thus, a circular orbit of a rotation trajectory represents a combination of spin about an axis and a precession about another axis (not necessarily perpendicular).

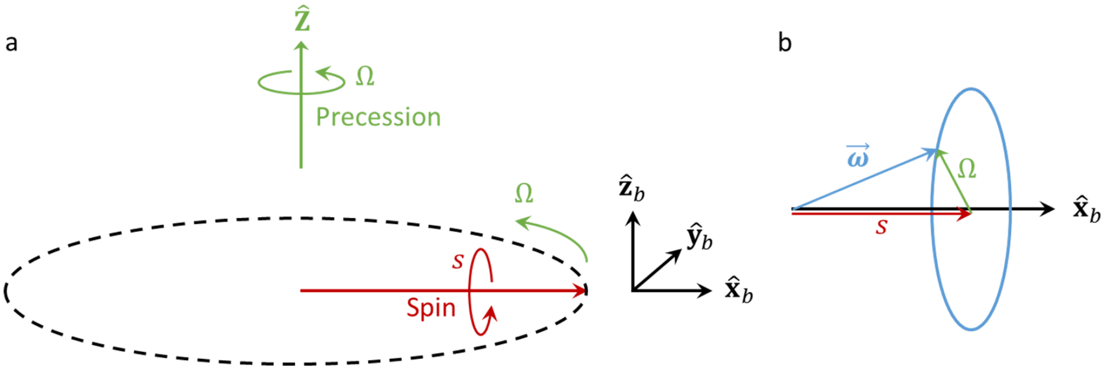

Figure 5-8 a) Illustration of rigid body undergoing spin and precession. b) A combination of spin and precession leads to a circular orbit in angular velocity space, thus explaining the observed rotation behavior from Figure 5-7.

Thus, the fragment tumbling dynamics can be explained. After initial transient motion, the fragments settle into a spin-precession state about either the maximum or minimum principal axes of inertia. By inspection of the rotation trajectories, it appears that the minimum axis is preferred. Note that the plots are relative to a body-fixed axis, so this does not include information on the principal axes orientation relative to the flight trajectory. The tumbling motion and preferred orientations relative to the inertial reference frame could be a subject of future investigation.

5.3. Trajectory Uncertainty Due to Initial Angular Velocity

In the previous sections, the fragment trajectories were investigated with zero initial angular velocity. However, upon fragment formation after detonation and case breakup, it is likely the fragments hold an initial angular velocity. Without advanced diagnostics, it is difficult to determine the initial angular velocity, but the results of this section show that understanding the initial rotation rate is important because it affects the trajectory distributions.

Since the initial rotation rate is currently not well understood, simulations were conducted to determine the resulting trajectories as a function of initial angular velocities spanning multiple orders of magnitude. Similar to the previous section, initial orientations were assumed to be equally likely and randomly sampled. The initial velocity was 2.5 km/s, but an additional constant angular velocity magnitude was imposed with a randomized initial rotation axis. 100 fragment trajectories were sampled, and this procedure was repeated for angular velocities ranging from 10^3 to 10^6 deg/s.

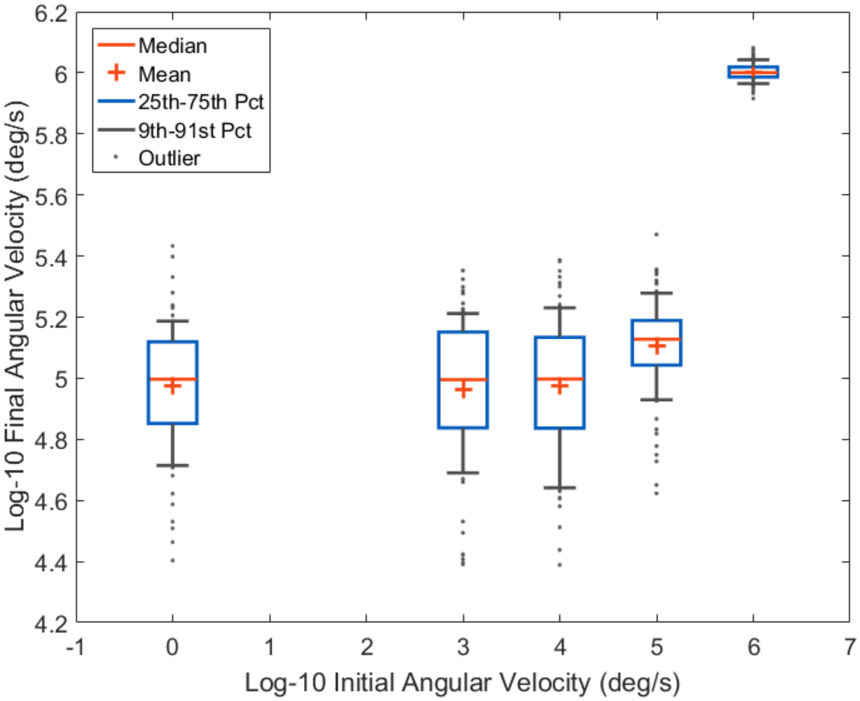

Figure 5-9 Box plots showing distributions of final angular velocity after fragment has decelerated to 1 km/s for various initial angular velocities. A zero angular velocity initial condition is listed under the value of 0 in the horizontal axis.

First, the final angular velocity distributions (after the fragment has slowed to 1 km/s) are shown in box plots for various initial rotation rates in Figure 5-9. From Figure 5-6, the most probable final angular velocity for no initial rotation was found to be approximately 10^5 deg/s. This will be referred to as the "steady tumbling rate." When the fragment initially spins with a rate below the steady tumbling rate, the final angular velocity distributions are nearly identical and centered around the steady tumbling rate. However, when the fragment has an initial angular velocity at or above the steady tumbling rate, the final rotation rate distributions change. At 10^5 deg/s initial rotation rate, the final rotation rate is slightly above the steady tumbling rate, and the spread has decreased. At 10^6 deg/s, the difference is clear — the final rotation rate is centered about the same initial rotation rate with a smaller percentage spread.

These patterns suggest that when the initial rotation rate is below the steady tumbling rate, the aerodynamic moments dictate the rotational dynamics and cause the fragment to spin up to the steady tumbling rate regardless of the initial angular velocity. When the initial rotation rate is above this threshold steady tumbling rate, the rotational inertia dominates, and the rotational kinetic energy does not have enough time to dissipate.

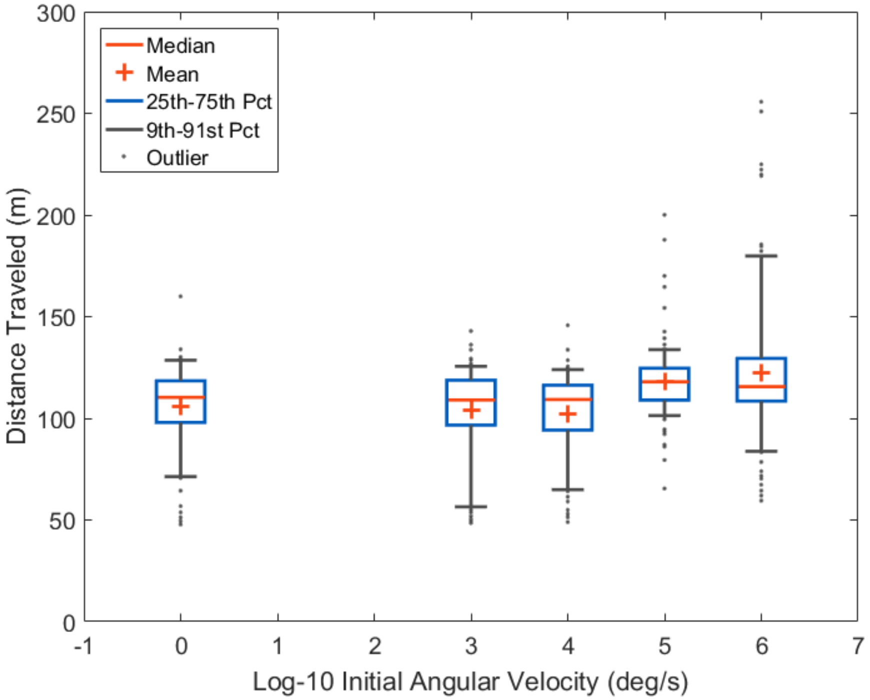

Figure 5-10 Box plots showing distributions of distance traveled after fragment has decelerated to 1 km/s for various initial angular velocities. A zero angular velocity initial condition is listed under the value of 0 in the horizontal axis.

To determine how the initial rotation rate affects the fragment flight trajectory, box plots in Figure 5-10 show the distributions of distance traveled after the fragment has slowed to 1 km/s for various initial rotation rates. Similar to Figure 5-9, the distance distributions are nearly identical for initial rotation rates below the steady tumbling rate of 10^5 deg/s. At or above the steady tumbling rate, the distance distributions have a slightly larger mean flight distance. More importantly though, the spread is much larger, and the distribution transitions from a left skew to a right skew. In this regime above the steady tumbling rate, more fragments are observed to fly farther. This can happen because the larger initial angular momentum can cause the fragment to stabilize in certain spin-precession states about the largest principal axis similar to a spinning Frisbee®. If the fragment is traveling in a direction that the thin edge is opposing the flow, the fragment would experience lower drag throughout the course of its trajectory.

5.4. Size Effects on Fragment Velocities

The effect of fragment size on its trajectories is investigated in this section. The fragment size is characterized by the longest length of the minimum-volume bounding box of the fragment. In order to simulate different sizes of the same fragment in Figure 2-1, the geometric and material properties are scaled properly. 100 sample trajectories of fragments of each specified size with randomized initial orientations and no initial angular velocities were simulated. The velocity was

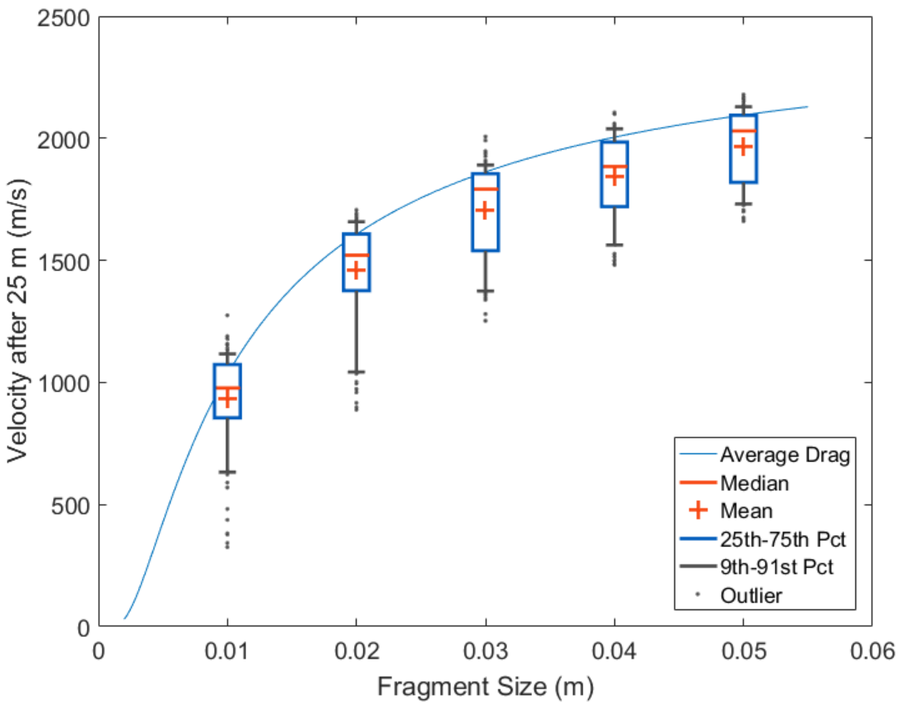

Figure 5-11 Box plots showing the distributions of velocity after the fragment has traveled 25 meters for various fragment sizes.

computed after the fragment traveled 25 meters with an initial velocity of 2.5 km/s. This process was repeated for fragments ranging in size from 1 cm to 5 cm.

In Figure 5-11, box plots show the distribution of final velocities as a function of fragment size. The plots show that the velocity decreases with decreasing fragment size. The distributions are left skewed, similar to that in Figure 5-4. The prediction of velocity vs. size using a single average drag coefficient is also plotted. This curve can be expressed as $v(L) = v_0 \exp(-C/L)$, where C is a constant proportional to the average drag coefficient (details in Appendix C). The single DOF solution is found to slightly over-predict the mean velocity. This is consistent with Figure 5-3 in which the single DOF solution approximates the most probable trajectory, but this lies above the mean because of the left skew. Furthermore, the exponential curve shows that smaller fragments can lose significant speed in a short distance.

The lateral drift distribution vs. fragment size is plotted in Figure 5-12. The plot shows that smaller fragments have slightly higher mean lateral drift and also an increased spread. One probable explanation is that the smaller fragments decelerate more quickly and thus take a longer time to travel the horizontal distance. This leads to a longer drift time and more opportunity to change course. There is also a competing effect. The slower speed of the fragment means that when the fragment does make a turn, it would also drift away more slowly than a larger fragment. The competing effects appear to balance out for a fragment size of 3 cm and higher. For example, the 3 cm fragment has almost 5 times less mass than the 5 cm fragment, but the lateral drift distribution stays almost the same between those sizes. Note that the fragment shape was

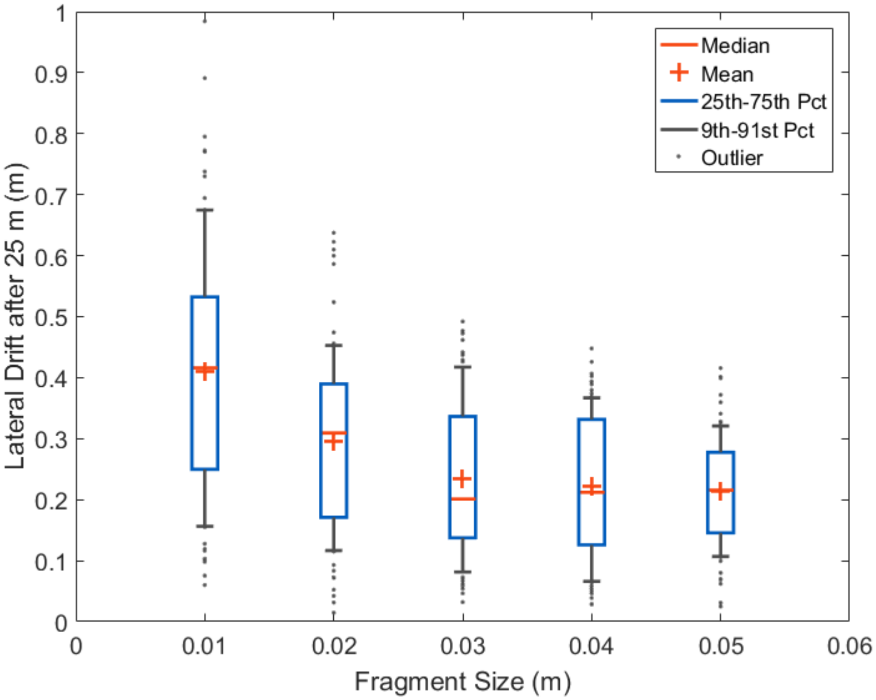

Figure 5-12 Box plots showing the distributions of lateral drift after the fragment has traveled 25 meters for various fragment sizes.

unchanged in this study. For fragments of different aspect ratios the lateral drift distributions may change.

Figure 5-13 also shows box plots that depict the final angular velocities as a function of fragment size. The plots show that the angular velocities decrease with increasing size, which confirms that the fragment moments of inertia decrease more quickly with fragment size than aerodynamic moments. Note that the unscaled fragment size of 4.4 cm is not shown in this plot, but as discussed earlier, it has a late-time steady tumbling rate of approximately 10^5 deg/s (Figure 5-6). By inspecting the box plot in Figure 5-13, the final angular velocity for the unscaled fragment after 25 meters is approximately 60,000 deg/s. After 25 m, the fragment has already attained 60% of its steady tumbling rate.

6. Summary and Outlook

Predicting the trajectories of explosive fragments is an important problem especially in the area of range safety. Modeling efforts and the understanding of the 6DOF fragment trajectories are currently limited. The simplest model uses a single drag coefficient and computes the trajectory without any knowledge of the rotational dynamics. On the other hand, a fully coupled solution that simultaneously solves both the flow field and rigid body motion is most accurate but computationally too expensive. Thus, a quasi-steady model is adopted in which the 6DOF

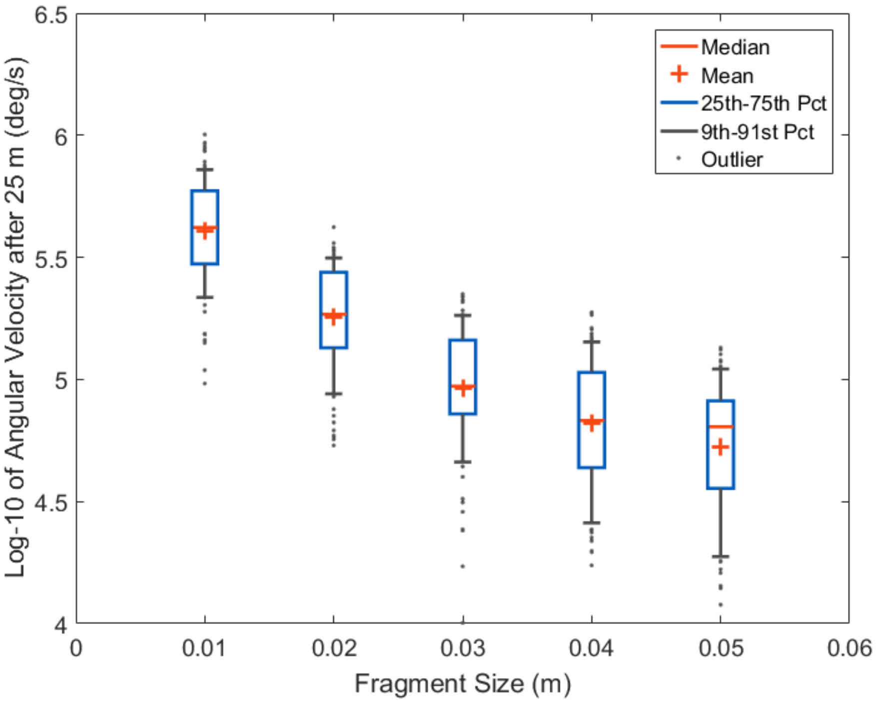

Figure 5-13 Box plots showing the distributions of angular velocity after the fragment has traveled 25 meters for various fragment sizes.

fragment trajectory is computed by integrating aerodynamic forces and moments from a database established using steady flow simulations sampled at multiple orientations.

Supersonic flow simulations were performed for simple geometries such as a 2D cylinder and a 3D cube. The computed aerodynamic coefficients were shown to match well with literature values. Then the full quasi-steady simulation procedure was performed for a generated test fragment. The fragment trajectories and tumbling mechanics were analyzed. The analysis shows that the 6DOF simulations can capture the spread of trajectories that the fragment can travel, while an average drag coefficient can approximate the most likely trajectory. After sufficient time and regardless of initial orientation and angular velocity, the fragment reaches a steady tumbling rate undergoing spin and precession about one of its 2 stable principal axes. If it spins about the largest principal axis, it might fly farther than expected due to a lower presented area. Varying the size of the fragment shows that larger fragments fly more quickly and drift less, while smaller fragments slow down more quickly and drift more on average at the same distance traveled.

Potential areas for future work are to a) validate the model with experimental data and b) automate and parallelize the entire simulation process in order to create a large data set characterizing the distance traveled for multiple fragments. The experiments would involve recording high speed videos of fragments that are shot through the air. Multiple cameras may be placed judiciously in order to record the position, velocity, and rotational characteristics of the fragment. The measured trajectories would be compared to the simulation results to establish the simulation accuracy. With accurate simulations, fragment trajectory characterization could be performed without excessive time consuming and expensive experimental tests. The automation effort would involve writing scripts and using software wrappers to transfer data seamlessly between different pieces of software. Ultimately, the trajectories and behaviors of fragments in flight would be statistically analyzed from a large data set and therefore be more clearly understood to aid in applications of interest.

References

[1] D. F. Gordon, B. Hafizi, Y.-Y. Khine, and S. Douglass. Ballistics modeling for non-axisymmetric hypervelocity smart bullets. Technical Report NRL/MR/6790–14-9549, Naval Research Laboratory, June 2014.

[2] S. G. Jennings. The mean free path in air. *Journal of Aerosol Science*, 19(2):159–166, 1988.

[3] P. Reu. Private communication.

[4] S. M. Murman, M. J. Aftosmis, and M. J. Berger. Simulations of 6-DOF motion with a Cartesian method. AIAA Paper 2003-1246, 41st AIAA Aerospace Sciences Meeting, January 2003.

[5] Sierra/Aero Development Team. SIERRA/Aero User Manual – Version 4.54. Technical Report SAND2019-12293, Sandia National Laboratories, 2019.

[6] Sierra/Aero Development Team. SIERRA/Aero Theory Manual – Version 4.54. Technical Report SAND2019-12292, Sandia National Laboratories, 2019.

[7] F. R. Menter. Two-equation eddy-viscosity turbulence models for engineering applications. *AIAA Journal*, 32(8):1598–1605, 1994.

[8] https://www.pointwise.com/.

[9] P. W. Cooper. *Explosives Engineering*. Wiley, 1996.

[10] V. A. Bashkin, A. V. Vaganov, I. V. Egorov, D. V. Ivanov, and G. A. Ignatova. Comparison of calculated and experimental data on supersonic flow past a circular cylinder. *Fluid dynamics*, 37(3):473–483, 2002.

[11] H. Goldstein, C.P. Poole, and J.L. Safko. *Classical Mechanics*. Addison Wesley, 2002.

[12] https://github.com/pointwise/shapewizard.

[13] CUBIT 15.5 User Documentation. Technical Report SAND2019-3478 W, Sandia National Laboratories, 2019.

APPENDIX A. Meshing Procedure

The meshing procedure applies to Pointwise [8], and the description assumes familiarity with the software terminology.

0. Set software parameters. Before beginning, set the grid dimension to "3D", the solver to "EXODUS II", and the grid type to "Unstructured."

1. Generate or import a fragment surface triangulation. For a simple shape such as a sphere, box, or an extrusion, the ShapeWizard plug-in [12] can quickly generate a domain with a triangular mesh. For a CAD geometry with a closed surface, import the CAD geometry into Pointwise as a database and create the connectors and triangular mesh domain from the database. For an arbitrary shaped fragment specified by facets such as STL files, the process is much more difficult. Unless the STL surface triangles can function as a suitable mesh, Pointwise is likely to have trouble sizing and meshing the surface. One possible solution is to use CUBIT [13], which contains more robust STL features. The `TriMesh` algorithm in CUBIT can often work to re-mesh faceted geometries with perhaps some geometry clean-up. The resulting surface mesh can be saved as an STL and imported into Pointwise as a domain.

2. Generate the far field domain. After the fragment domain is successfully imported or generated in Pointwise, use ShapeWizard to quickly generate a spherical far field surface triangulation with radius approximately 4.5 times the characteristic length of the fragment. Use a spacing no more than 4 times the spacing of the fragment domain.

3. Extrude the fragment domain. This is an optional step for improved stability and accuracy, especially for some objects with sharp corners. Extrude the fragment surface outward with approximately 10–20 steps to create wedge layers.

4. Initialize a block in the interior space. Select the far field domain and the outer wedge layer domain. Then assemble and initialize a block. This step will create a tetrahedral volume mesh and may take significant compute time.

5. Create and label side set boundary conditions. Label the far field domain `farfield` and the fragment surface domain `wall`. These are chosen to match the example input script in Appendix B.

6. Export as EXODUS file. Select all blocks, domains, and connectors. Export as "CAE", which will save an EXODUS file to be used with SIERRA/Aero.

APPENDIX B. Sample SIERRA/Aero Input File

The following is an example input file for SIERRA/Aero to compute the flow field at a single fragment orientation at Mach 3. Specific file names have been omitted and replaced with placeholders:

- `[MESHNAME]` — EXODUS input mesh file
- `[DATARESTART]` — SIERRA/Aero restart file name
- `[DATAOUT]` — EXODUS output data file

```
Begin Sierra FlowFrag

$--------------------------------------------------------
$   Procedure domain - solution control, region settings
$--------------------------------------------------------

  Begin Conchas Procedure AeroProcedure

$---------------------------------------------------
$     Define temporal solution parameters
$---------------------------------------------------
    Incremental Steps = 4000
    Begin Run Schedule
      ITs  step_type      ramp_type   ramp  step_max  step  spatial_order  max_pi  limiter
      1    cfl_local_dt   increment   0.01  20        2     first          6       node_va
      401  cfl_local_dt   increment   0.01  20        2     second         6       node_va
    end

$------------------------------------------------------
$     Region domain - EQs, BCs, ICs, post-processing
$------------------------------------------------------

    Begin Conchas Region AeroRegion

$---------------------------------------------------
$       Specify mesh name and decomposition
$---------------------------------------------------
      Mesh Database Name = [MESHNAME]
      Mesh Decomposition Method = RIB

$---------------------------------------------------
$       Define material properties to be used
$---------------------------------------------------
      Begin Gas Properties
        Gamma         = 1.4
        Specific_r    = 287.097384767
        Sutherland_c1 = 1.458e-06
        Sutherland_c2 = 110.4
        Prandtl       = 0.72
      End   Gas Properties

$--------------------------------------------------------
$       Solution options - equations, solver options
$--------------------------------------------------------

      Begin Solution Options

$---------------------------------------------------
$         Specify equations to solve
$---------------------------------------------------
        Activate Equation NavierStokes
```

```
$----------------------------------------------------------
$         Define additional variables to post-process
$----------------------------------------------------------
        Post Process yplus on wall
        Post Process mach_number on all_blocks

$--------------------------------------------------
$         Define turbulence model parameters
$--------------------------------------------------
        Begin Turbulence model Specification SST
          Turbulence Model = SST
          Clip Turbulence Variables
        End   Turbulence model Specification SST

$--------------------------------------------------
$         Other options
$--------------------------------------------------
        Inviscid Flux Type = MSW
        Gradient Method = WeightedLeastSquares

      End   Solution Options

$--------------------------------------------------
$       Specify flow state variables
$--------------------------------------------------
      Begin Flow State Infinity
        Pressure    = 101325.0
        Temperature = 298.0
        Mach Number = 3.0
        Direction   = -1.0, 0.0, 0.0
        Turbulence Intensity = 0.01
        Turbulent Viscosity Ratio  = 0.1
      End   Flow State Infinity

$--------------------------------------------------
$       Specify initial conditions
$--------------------------------------------------
      Begin Initial Condition Block FlowInit
        All Volumes
        Use Flow State Infinity
      End   Initial Condition Block FlowInit

$--------------------------------------------------
$       Specify boundary conditions
$--------------------------------------------------

      # Far - Farfield
      Begin Characteristic Projection on Surface farfield
        TYPE is farfield
        Use Flow State Infinity
      End Characteristic Projection on Surface farfield

      # Frag Surface - Wall
      Begin Wall Boundary Condition on Surface wall
      End   Wall Boundary Condition on Surface wall

$--------------------------------------------------
$       Calculate force and moment on walls
$--------------------------------------------------
      Begin Force and Moment FoMo
        Moment Center = 0, 0, 0
        Use Solid Walls
         Split Contributions
      End   Force and Moment FoMo

$--------------------------------------------------------
$       Define parameters for checkpoint/restart file
$--------------------------------------------------------
```

```
      Begin Restart Output
        Database Name = [DATARESTART]
        At Step 0, Increment = 500
      End   Restart Output

      Begin Restart Input
        Database Name = [DATARESTART]
#         activate restart
#         restart instance = 1
      End   Restart Input

$---------------------------------------------------
$       Define contents of binary plot file
$---------------------------------------------------
      Begin Results Output Label AeroOutput
        Database Name = [DATAOUT]
        At Step 3000, Increment = 1000
        Nodal Variable = Density as rho
        Nodal Variable = Pressure as P
        Nodal Variable = Velocity as U
        Nodal Variable = Temperature as T
        Nodal Variable = Turbulent_Kinetic_Energy as TKE
        Nodal Variable = Turbulent_Dissipation as SDR
        Nodal Variable = Turbulent_Viscosity as muT
        Nodal Variable = Yplus as yPlus
        Nodal Variable = MACH_NUMBER as Ma
      End   Results Output Label AeroOutput

    End   Conchas Region AeroRegion

  End   Conchas Procedure AeroProcedure

End   Sierra FlowFrag
```

APPENDIX C. Fragment Trajectory with a Single Drag Coefficient

This appendix documents the solution of a fragment trajectory with a single drag coefficient.

Consider a rigid fragment with mass m, volume V, density $\rho_s = m/V$, and surface area A. It travels in a fluid with density ρ, and its trajectory can be characterized by velocity v, position r, and time t. Generally, the drag $C_D(\alpha, \beta_E)$ depends on orientation relative to its velocity vector.

C.1. Computing Average Drag Coefficient

The average drag $\overline{C_D}$ is computed by averaging over a spherical surface and can be expressed analytically as

$$\overline{C_D} = \frac{1}{4\pi} \int_{-\frac{\pi}{2}}^{\frac{\pi}{2}} \int_{-\pi}^{\pi} C_D(\alpha, \beta_E) \cos \beta_E \, \mathrm{d}\alpha \, \mathrm{d}\beta_E \tag{C.1}$$

For sampled pairs of $(\alpha, \beta_E)^i$ with evenly spaced angles $\Delta\alpha^i$ and $\Delta\beta_E^i$, this integral can be approximated as

$$\overline{C_D} \approx \frac{1}{4\pi} \sum_i C_D(\alpha, \beta_E)^i \cos \beta_E^i \Delta\alpha^i \Delta\beta_E^i \tag{C.2}$$

This average drag $\overline{C_D}$ is used for a single drag coefficient approximation.

C.2. Governing Equations

By Newton's Second Law and expressing drag as proportional to the square of the velocity, the governing equations to solve for $v(t)$, $v(r)$, and $r(t)$ are

$$m \frac{\mathrm{d}v}{\mathrm{d}t} = -bv^2 \tag{C.3}$$

$$mv \frac{\mathrm{d}v}{\mathrm{d}r} = -bv^2 \tag{C.4}$$

$$m \frac{\mathrm{d}^2 r}{\mathrm{d}t^2} = -b \left(\frac{\mathrm{d}r}{\mathrm{d}t} \right)^2 \tag{C.5}$$

where

$$b = 0.5 \overline{C_D} \rho A \tag{C.6}$$

C.3. Velocity vs. Time

With initial condition $v(t=0)=v_0$, the solution to equation C.3 is

$$v(t)=\frac{v_0 m}{v_0 b t+m} \tag{C.7}$$

C.4. Velocity vs. Position

With initial condition $v(r=0)=v_0$, the solution to equation C.4 is

$$v(r)=v_0\exp\left(-\frac{b}{m}r\right) \tag{C.8}$$

C.5. Position vs. Time

With initial conditions $v(t=0)=v_0$ and $r(t=0)=0$, the solution to equation C.5 is

$$r(t)=\frac{m}{b}\ln\left(\frac{v_0 b}{m}t+1\right) \tag{C.9}$$

C.6. Velocity Scaling with Size

This section shows how velocity scales with fragment size for a fixed flight distance d.

From equation C.4, substitute for b and m:

$$v=v_0\exp\left(-\frac{0.5\rho\overline{C_D}A}{\rho_s V}d\right) \tag{C.10}$$

Define characteristic fragment length L, which for example, can be the fragment minimum bounding box longest side length. The volume and surface area then scale with L as $V=c_1L^3$ and $A=c_2L^2$. Substituting into C.10 yields

$$v(L)=v_0\exp\left(-\frac{C}{L}\right) \tag{C.11}$$

where C is a constant, given by

$$C\equiv\frac{0.5\rho\overline{C_D}dc_2}{\rho_s c_1} \tag{C.12}$$

DISTRIBUTION

Email—Internal (encrypt for OUO)

Name	Org.	Sandia Email Address
Technical Library	01977	libref@sandia.gov

Sandia National Laboratories